



Published in final edited form as:

Cell Rep. 2021 December 07; 37(10): 110098. doi:10.1016/j.celrep.2021.110098.

Neurexin-3 defines synapse- and sex-dependent diversity of GABAergic inhibition in ventral subiculum

Emma E. Boxer^{1,2}, Charlotte Seng³, David Lukacsovich³, JungMin Kim^{1,2}, Samantha Schwartz¹, Matthew J. Kennedy¹, Csaba Földy³, Jason Aoto^{1,4,*}

¹University of Colorado Anschutz, Department of Pharmacology, Aurora, CO 80045, USA

²Neuroscience Graduate Program, University of Colorado Anschutz, Aurora, CO 80045, USA

³Laboratory of Neural Connectivity, Brain Research Institute, Faculties of Medicine and Science, University of Zurich, 8057 Zurich, Switzerland

⁴Lead contact

SUMMARY

Ventral subiculum (vSUB) is integral to the regulation of stress and reward; however, the intrinsic connectivity and synaptic properties of the inhibitory local circuit are poorly understood. Neurexin-3 (Nrxn3) is highly expressed in hippocampal inhibitory neurons, but its function at inhibitory synapses has remained elusive. Using slice electrophysiology, imaging, and single-cell RNA sequencing, we identify multiple roles for Nrxn3 at GABAergic parvalbumin (PV) interneuron synapses made onto vSUB regular-spiking (RS) and burst-spiking (BS) principal neurons. Surprisingly, we find that intrinsic connectivity of vSUB and synaptic function of Nrxn3 in vSUB are sexually dimorphic. We reveal that PVs make preferential contact with RS neurons in male mice, but BS neurons in female mice. Furthermore, we determine that despite comparable Nrxn3 isoform expression in male and female PV neurons, Nrxn3 knockout impairs synapse density, postsynaptic strength, and inhibitory postsynaptic current (IPSC) amplitude at PV-RS synapses in males, but enhances presynaptic release and IPSC amplitude in females.

Graphical abstract

This is an open access article under the CC BY-NC-ND license (<http://creativecommons.org/licenses/by-nc-nd/4.0/>).

*Correspondence: jason.aoto@cuanschutz.edu.

AUTHOR CONTRIBUTIONS

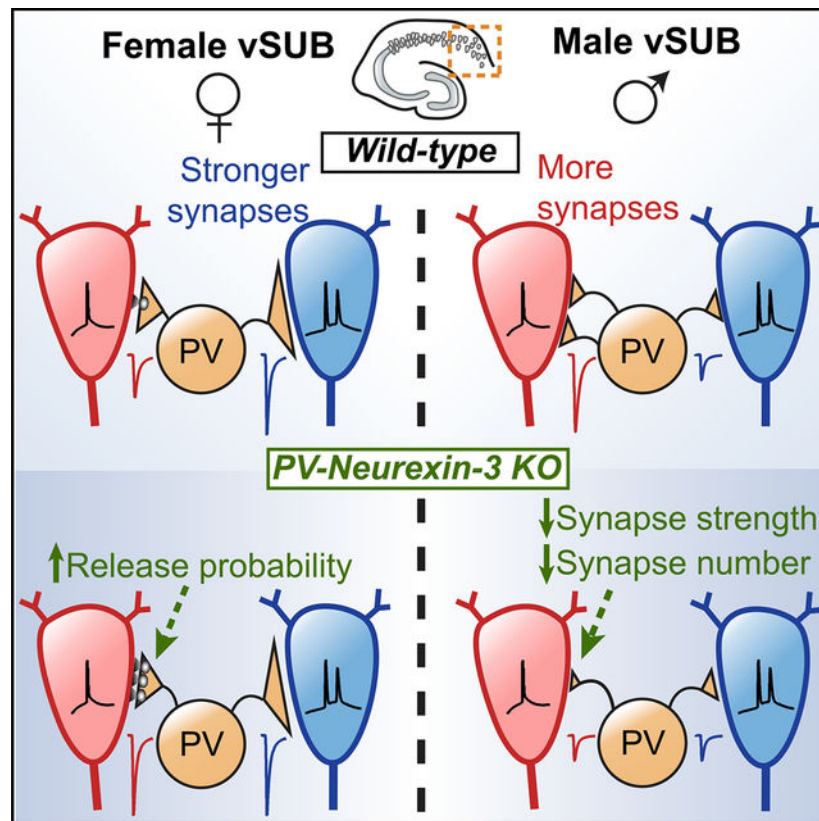
E.E.B. performed AAV injections electrophysiology and synapse imaging, collected and prepared PV mRNA, and performed data analysis. C.S. and D.L. performed RNA sequencing and analysis in the lab of C.F. J.K. performed PV density studies and electrophysiology analysis. S.S. wrote MATLAB code for the PV synapse quantification in the lab of M.J.K. E.E.B. and J.A. are responsible for study conception, experimental design, and data interpretation. E.E.B. and J.A. wrote the manuscript with input from all authors.

SUPPLEMENTAL INFORMATION

Supplemental information can be found online at <https://doi.org/10.1016/j.celrep.2021.110098>.

DECLARATIONS OF INTERESTS

The authors declare no competing interests.



In brief

While the diverse role of neurexins at hippocampal excitatory synapses is becoming more clear, the function of neurexins at hippocampal inhibitory synapses is less well known. Boxer et al. reveal that at parvalbumin inhibitory synapses, neurexin-3 function and local circuit connectivity are cell-type- and sex-specific within the ventral subiculum circuit.

INTRODUCTION

Precise innervation and synaptic transmission properties of local GABAergic interneurons with principal neurons are essential for faithful information processing and behavior, and disruption of inhibitory activity underlies many aspects of neuropsychiatric, neurodevelopmental, and substance use disorders (SUDs). Synaptic cell adhesion molecules play a critical role in specifying and maintaining synaptic inhibition, and mutations in genes that encode for these molecules are often linked to brain disorders. Neurexins (Nrxns) are a family of essential and evolutionarily conserved presynaptic cell adhesion molecules that engage in transsynaptic interactions with an expanding number of postsynaptic ligands to control presynaptic and postsynaptic properties of synaptic transmission (Südhof, 2017). However, the cell-type- and synapse-specific roles Nrxns perform remain enigmatic. Furthermore, stunning sex differences in the prevalence and symptomology of neuropsychiatric disorders such as schizophrenia (SCZ) and SUDs (Becker, 2016; Hoffman

et al., 2021; Leung and Chue, 2000) raise the possibility that adhesion molecule usage in SCZ and SUD-relevant circuits is sexually dimorphic.

Nrxns are encoded by three genes (*NRXN1–3*), which make α , β , or the Nrxn1-specific γ isoforms from independent promoters and are alternatively spliced at six conserved splice sites (SS1–6). While Nrxn1–3 exhibit high sequence homology, share common binding partners, and display some compensatory behavior (Aoto et al., 2015; Südhof, 2017), recent evidence supports the hypothesis that individual Nrxns play functionally distinct roles in synaptic transmission (Aoto et al., 2015; Dai et al., 2019, 2021). This is further supported by the highly variable expression patterns of Nrxn isoforms and alternative splice variants across brain regions and among neuron cell types (Aoto et al., 2013; Földy et al., 2016; Fuccillo et al., 2015; Lukacsovich et al., 2019). These differential expression profiles and their combinatorial interactions with postsynaptic ligands are thought to specify excitatory and inhibitory synapse formation and confer distinct function (Aoto et al., 2015; Dai et al., 2019; Südhof, 2017). A recent study observed sex-dependent changes in Nrxn3 expression and alternative splicing in mouse hippocampus following chronic stress, suggesting that Nrxn3 may engage in sex-specific functions in hippocampus (Freire-Cobo and Wang, 2020). However, previous studies focusing on functional characterization of Nrxns have not considered sex as an independent variable.

In hippocampus, Nrxn3 mRNA is highly expressed in GABAergic neurons and exhibits differential isoform expression in distinct interneuron classes (Fuccillo et al., 2015; Ullrich et al., 1995). Additionally, neuroligin-2, a prototypical Nrxn ligand localized to inhibitory synapses, exhibits the highest binding affinity for Nrxn3 β *in vitro* (Koehnke et al., 2010). Thus, it was surprising that manipulation of Nrxn3 in developing dissociated hippocampal culture did not alter inhibitory synaptic transmission (Aoto et al., 2013, 2015; Restrepo et al., 2019). Although untested, Nrxn3 may instead impart functional relevance to mature intact hippocampal inhibitory microcircuits where cell-type-specific connectivity is preserved. Unique from *NRXN1* and *NRXN2*, *NRXN3* mutations are primarily associated with SUDs, SCZ, and stress disorders in humans and animal models (Brown et al., 2011; Hishimoto et al., 2007; Kelai et al., 2008; Lachman et al., 2007; Liu et al., 2006; Novak et al., 2009), suggesting that Nrxn3 may dominantly and sex specifically regulate synaptic properties of neural circuits implicated in these disorders, such as ventral subiculum (vSUB).

vSUB is an understudied subregion of the hippocampal formation that is integral to the regulation of stress, fear, and reward behaviors via its projections to cortical and subcortical regions (Grace, 2010). vSUB hyperexcitability is commonly observed in SCZ, SUDs, and depression in animal models and human patients, and it is thought to arise from fast-spiking parvalbumin (PV)-expressing interneuron dysfunction (Gill and Grace, 2014; Grace, 2010; Konradi et al., 2011). Of interest, PV neurons in hippocampus control sharp-wave ripple oscillatory activity relevant to learning (Schlinghoff et al., 2014) and express Nrxn3 at significantly higher levels than Nrxn1 and Nrxn2 (Nguyen et al., 2016; Que et al., 2021), suggesting that Nrxn3 may perform a critical, yet unidentified, role in establishing and defining PV interneuron-dependent inhibition within the circuit. Relative to other hippocampal subregions, where local inhibitory architecture is well defined from decades of studies in male rodents, the inhibitory cell types and patterns of connectivity in

vSUB have remained largely enigmatic (Böhm et al., 2018). However, the properties and connectivity patterns of subicular regular-spiking (RS) and burst-spiking (BS) pyramidal neurons have been more thoroughly described. RS and BS neurons are discrete classes of pyramidal neurons that possess striking differences in physiology and brain connectivity and likely mediate distinct behaviors (Cembrowski et al., 2018; Graves et al., 2012; Kim and Spruston, 2012; Wee and MacAskill, 2020; Wozny et al., 2008). Determining the functional organization of PV input onto RS and BS neurons and investigating what role *Nrxn3* plays at PV inhibitory synapses in vSUB may elucidate mechanisms that underlie aberrant vSUB activity observed in SCZ and SUDs.

Here, we uncover unexpected sexually dimorphic patterning of PV connections in vSUB and identify a role for *Nrxn3* in mediating inhibitory synaptic transmission in a sex- and cell-type-specific manner. Using optogenetics, paired recordings, mouse genetics, and imaging, we show that PVs preferentially synapse onto RS neurons in males, but BS neurons in females. We find that *Nrxn3* knockout (KO) in PV neurons drastically reduces PV inhibitory postsynaptic currents (IPSCs) in RS neurons in males, driven by a reduction in PV synapse number and postsynaptic strength. In females, PV *Nrxn3* KO leads to a robust enhancement of IPSCs, which is facilitated by an increase in release probability, revealing an unexpected role for *Nrxn3* in suppressing GABA release. Lastly, using single-cell RNA sequencing (scRNA-seq), we find high expression levels of *Nrxn3 α* and *Nrxn1 γ* in PV neurons, but despite sex-specific *Nrxn3* KO effects, we detect no sex differences in *Nrxn* alternative splicing or isoform expression in vSUB PV neurons.

RESULTS

PV interneurons exhibit cell-type- and sex-dependent inhibitory bias in the basal subicular microcircuit

To begin to systematically characterize PV inhibition in male and female vSUB, we injected AAV-DIO-ChIEF, a cre-dependent Channelrhodopsin variant, into vSUB of P21 PV-Cre mice. 14–21 days later, we prepared acute *ex vivo* slices and performed whole-cell recordings to assess light-evoked PV inhibitory postsynaptic currents (PV-IPSCs) in electrophysiologically identified RS and BS neurons (Figures 1A–1C). We performed input/output (I/O) experiments to measure total PV synaptic drive and paired-pulse ratio (PPR) experiments to assess presynaptic release probability. Surprisingly, we found that the functional connectivity of PVs with RS and BS neurons is sexually dimorphic. In female vSUB, the PV-IPSC I/O slope was 121% greater for BS neurons compared to RS neurons (Figure 1D). In contrast, in males, the PV-IPSC I/O slope was greater for RS neurons compared to BS neurons (by 84%, Figure 1F), consistent with previous reports (Böhm et al., 2015). Presynaptic release probability was similar at PV-RS and PV-BS synapses in either sex (Figures 1E and 1G). To our knowledge, vSUB is not generally thought of as a sexually dimorphic structure. Thus, we sought to determine the properties underlying the basal sex-specific patterning of PV inhibitory drive in detail.

Intrinsic properties of PV interneurons do not exhibit sexual dimorphism

To test whether the sex-specific phenotype was mediated by differences in the number of PV neurons and/or intrinsic excitability, we bred PV-Cre mice to a tdTomato reporter line, Ai9, to facilitate the selective identification of PV interneurons. We first quantified the number of tdTomato⁺ cells and found similar densities in male and female vSUB (Figure 2A). We next investigated whether sex-dependent differences in excitability exist. We performed whole-cell recordings from PV neurons in vSUB (Figure 2B) and monitored spontaneous excitatory postsynaptic currents (sEPSCs), resting membrane properties, and action potential (AP) properties. The frequency and amplitude of sEPSCs were similar in male and female PV neurons (Figure 2C). Furthermore, we did not observe differences in resting membrane properties between females and males (Table S1). We observed a slightly greater AP half-width in males, but no differences in AP frequency, AP kinetics, rheobase, or sag (Table S1; Figures 2D and 2E). Together, release probability, PV excitability, and PV cell number in vSUB are not sexually dimorphic and likely do not confer the sex-specific patterning of PV inhibitory drive among RS/BS neurons. Thus, differences in synaptic properties likely underlie the asymmetric inhibition by PV interneurons observed in both male and female vSUB.

Sex-specific patterning of vSUB PV-RS and PV-BS preference is mediated by synaptic density in males and postsynaptic strength in females

What synaptic properties contribute to the sex-dependent and cell-type-specific differences in PV-IPSC amplitudes in vSUB? IPSC amplitude is the product of presynaptic release probabilities, postsynaptic strengths, and number of synaptic contacts. Similar PV-IPSC PPRs in male and female RS and BS neurons indicate that release probability is not a factor in the cell-type-specific inhibition bias. To examine whether postsynaptic strength and/or synapse numbers are cell type specific and sexually dimorphic, we utilized strontium-mediated PV asynchronous IPSCs (PV-aIPSCs) to test for changes in postsynaptic strength and viral labeling to quantify PV synapses.

First, we measured light-evoked strontium-mediated PV-aIPSC amplitudes in *ex vivo* slices from male and female PV-Cre mice injected with AAV-DIO-ChIEF-mRuby (Figures 3A–3C). aIPSCs are analogous to miniature synaptic events, and aIPSC amplitude is thought to reflect postsynaptic strength (Bekkers and Clements, 1999). In females, PV-BS aIPSC amplitudes were 30% larger than PV-RS amplitudes (Figure 3D), indicating that PV postsynaptic strength is greater in BS neurons. In contrast, we observed no differences in PV-aIPSC amplitude in males (Figure 3E). To evaluate PV synapse density, we injected a cre-dependent bicistronic adeno-associated virus (AAV) expressing a membrane-tethered GFP to label processes and synaptophysin-mRuby to label putative presynaptic sites (AAV-DIO-mGFP-2A-SyPhy-mRuby) (Beier et al., 2015) into vSUB of PV-Cre mice (Figure 3F). We filled RS and BS neurons with biocytin, then imaged and quantified the total volume of mRuby⁺ PV boutons contacting perisomatic regions of 3D reconstructed RS and BS neurons (Figures 3G and 3H). We quantified total synaptic volume, normalized to the cell fill volume, as a proxy for synapse density, to account for overlapping synapses. As previously reported (Harris et al., 2001), the somatic volumes of RS and BS neurons were equal among all conditions (Figure S1). We found no difference in the density of PV synaptic inputs

onto RS and BS neurons in female vSUB (Figure 3I) but quantified more than twice as many PV synapses made onto RS relative to BS neurons in male vSUB (Figure 3J). Taken together, these results reveal that PV interneuron connectivity and basal synaptic properties are sexually dimorphic and cell type specific: in female vSUB, BS neurons receive greater PV-mediated inhibition due to greater postsynaptic strength, whereas in male vSUB, RS neurons receive greater PV-mediated inhibition due to increased synapse number.

Nrxn3 exerts sex-dependent and synapse-specific effects at PV-RS and PV-BS synapses in vSUB

Next, we asked whether Nrxn3 controls PV-mediated synaptic transmission in vSUB. We crossed PV-Cre mice with Nrxn3 $\alpha/\beta^{fl/fl}$ mice (PV-Nrxn3 KO) (Figure 4A) to selectively delete Nrxn3 from PV-expressing neurons at around post-natal day (P)9 (Taniguchi et al., 2011). We injected AAV-DIO-ChIEF into vSUB of PV-Nrxn3 KO and PV-Cre control mice (control mice were separately analyzed in Figure 1 for basal circuit characterization), then measured light-evoked PV-IPSCs in *ex vivo* slices (Figures 4B–4D). Intriguingly, PV-Nrxn3 KO resulted in profoundly distinct and sexually dimorphic phenotypes between RS and BS neurons. In females, PV-Nrxn3 KO at PV-RS synapses resulted in a 2-fold enhancement of PV-IPSC I/O slope and increased presynaptic release probability (Figures 4E and 4F). At PV-BS female synapses, we observed a minor reduction in the I/O relationship concurrent with a paradoxical 13% decrease in PPR (Figures 4G and 4H). Conversely in males, loss of Nrxn3 at PV-RS synapses reduced synaptic strength by 55% (Figure 4I), whereas PV-BS IPSCs were unaltered (Figure 4K). Deletion of Nrxn3 from PV neurons did not alter PV-IPSC PPRs in males nor PV-IPSC rise or decay kinetics in either sex (Figures 4J, 4L, and S2). These results reveal that Nrxn3 performs distinct and unexpected sex-dependent synaptic functions at PV-RS synapses: Nrxn3 KO produced a PV-IPSC gain-of-function phenotype in females and loss-of-function phenotype in males. The presynaptic gain-of-function observed in female PV-RS synapses identifies a role for Nrxn3 in suppressing GABA release at these synapses.

Synaptically connected paired recordings reveal sex- and synapse-specific roles of PV Nrxn3

To gain greater insight into the role of PV neurons in vSUB microcircuit, we performed paired whole-cell recordings between synaptically coupled presynaptic PV neurons and postsynaptic RS or BS cells in *ex vivo* slices from PV-Cre or PV-Nrxn3 KO mice. In contrast to our optogenetic approach, paired recordings allow us to precisely monitor unitary PV-IPSCs (uIPSCs) evoked from a single PV interneuron and thus offer a high-resolution assessment of synaptic transmission. We identified presynaptic PV neurons visually using either PV-Cre::Ai9 mice or PV-Cre or PV-Nrxn3 KO mice injected with AAV-DIO-mRuby, and validated their fast-spiking profile electrophysiologically (Figures 5A and 5B). We then tested the connectivity rate (connected pairs/total pairs tested) and connection strength (uIPSC amplitude, PPR, and failure rate) made onto neighboring principal neurons (Figure 5C). Deletion of Nrxn3 did not alter PV neuron excitability, as intrinsic membrane properties were unchanged (Figures S3A–S3D).

Consistent with our optogenetic results, in female PV-RS pairs, PV-Nrxn3 KO resulted in a striking 176% enhancement of uIPSC amplitude, and a decrease in PPR and uIPSC failure rate, indicating that increased presynaptic release probability likely contributes to the PV-IPSC gain of function at these synapses (Figures 5D, 5E, and S3E). In female PV-BS pairs, we observed an insignificant decrease in uIPSC amplitudes in PV-Nrxn3 KO animals and no change in either PPR or connectivity rate (Figures 5F and 5G). Also consistent with our optogenetic data, we observed a significant 69% reduction in uIPSC amplitude at male KO PV-RS synapses (Figures 5H and 5I). The reduction in uIPSC amplitude was not accompanied by changes in PPR; instead, we found that the rate of PV-RS connectivity was significantly reduced (Figure 5I). In male PV-BS pairs, uIPSC amplitudes, PPR, and connectivity rate were unaltered (Figures 5J and 5K). In all conditions, PV synapses exhibited low uIPSC failure rates (Figures S3E and S3I), indicative of high fidelity of release characteristic of PV interneurons (Bartos and Elgueta, 2012). Ablation of Nrxn3 from PV interneurons did not result in sex-dependent or synapse-specific changes to uIPSC kinetics, indicating that Nrxn3 does not control postsynaptic receptor composition at these synapses (Figures S3F–S3H and S3J–S3L). Taken together, the paired recording data reproduced the sexually dimorphic PV-Nrxn3 KO effect on PV-IPSC amplitude that we observed using ChIEF stimulation, and they suggest that the gain-of-function PV-IPSC phenotype at female PV-RS synapses is driven by increased release probability whereas the loss-of-function phenotype at male PV-RS synapses might be attributable to changes in synaptic connectivity.

Nrxn3 controls PV postsynaptic strength and synapse number in a cell-type- and sex-dependent manner

To further evaluate the synaptic properties controlled by Nrxn3 in PVs, we utilized strontium and imaging experiments detailed previously (Figure 3) to assess synaptic strength and synaptic density in PV-Cre (control) and PV-Nrxn3 KO animals. First, we measured light-evoked, strontium-mediated PV-aIPSCs in *ex vivo* slices. In females, PV-aIPSC amplitudes in RS and BS neurons were unaltered in PV-Nrxn3 KO animals (Figures 6A and 6B). In males, however, PV-aIPSC amplitudes were reduced in RS, but not BS, neurons, indicating that Nrxn3 controls postsynaptic inhibitory strength specifically at RS synapses (Figures 6C and 6D).

To examine whether Nrxn3 controls PV synapse density, we quantified PV synapses made onto RS and BS neurons (as described in Figures 3F–3H) and observed further sex- and synapse-specific roles for PV-Nrxn3. We found that Nrxn3 ablation from PV neurons did not alter synapse density on RS neurons in females (Figure 6E), suggesting that increased PV inhibition onto RS neurons is solely a result of enhanced release probability (Figure 5E). In contrast, at female PV-BS synapses, loss of Nrxn3 produced a significant reduction in synapse density (Figure 6F). Importantly, this effect appears to have been partially compensated by the small increase in release probability, which led to an insignificant reduction in IPSC amplitudes at BS synapses (Figures 4G, 4H, and 5G). In males, consistent with reduced connection probability at PV-RS synapses (Figure 5I), there were significantly fewer PV synapses on RS neurons in KOs compared to control (Figure 6G), but no change onto BS neurons (Figure 6H). Taken together, the functional analyses surprisingly revealed

that *Nrxn3* plays pleiotropic roles in PV interneurons in vSUB in a manner dependent on sex and post-synaptic cell type. At PV-RS synapses, *Nrxn3* suppresses PV presynaptic release in females, but promotes both postsynaptic strength and synapse density in males. At female PV-BS synapses, similar to male PV-RS synapses, *Nrxn3* promotes synapse density but appears to be dispensable at male PV-BS synapses. These findings raise the fascinating possibility that distinct *Nrxn3* isoforms or alternative splice variants exhibit sexually dimorphic expression patterns in PV neurons to manifest the disparate functional properties.

***Nrxn* isoform expression and alternative splicing in vSUB PVs are comparable between sexes**

To investigate whether differential *Nrxn* expression in PV interneurons contributes to the functional phenotypes observed in male and female vSUB, we harvested fluorescent and electrophysiologically validated single PV neurons from slices made from P35–42 female and male PV-Cre::Ai9 mice and performed scRNA-seq (Figure 7A). Each cell was inspected for RNA quality, yielded high mapping rates (Figures 7B and S5A), and displayed high levels of PV expression along with other gene markers typical of PV basket cells (Figure S5C) (Que et al., 2021).

Surprisingly, we did not observe significant sex differences in *Nrxn* expression in vSUB PVs (Figure 7C). Both male and female PVs exhibited high overall levels of *Nrxn1* and *Nrxn3* and relatively low levels of *Nrxn2* expression. High levels of *Nrxn1* were unexpected, as other groups have reported *Nrxn3* to be the most abundant *Nrxn* in CA1 PV cells (Nguyen et al., 2016; Que et al., 2021). This led us to investigate the expression of *Nrxn* isoforms in vSUB PV neurons (Figure 7D). We found that the primary *Nrxn* isoforms expressed are *Nrxn1 γ* and *Nrxn3 α* (Figures 7E and S5B). *Nrxn1 γ* is a highly truncated *Nrxn* isoform with no known role at mammalian synapses (Figure 7D) (Sterky et al., 2017). In contrast, *Nrxn3 α* contains a full complement of extra-cellular domains and is able to engage in transsynaptic interactions. Supported by our functional interrogation, this suggests that *Nrxn3 α* dominantly controls synaptic properties of PV neurons in vSUB. We also examined the splice site inclusion rates for *Nrxn1–3*. We found that alternative exon usage was similar to previous reports from cortex and CA1, indicating that PV neurons exhibit remarkably consistent *Nrxn* splicing across brain regions (Figure 7F) (Fuccillo et al., 2015; Lukacovich et al., 2019; Nguyen et al., 2016; Que et al., 2021). Transcriptomes of male and female PV neurons were virtually identical with the exception of seven differentially expressed genes (Figures 7G and 7H; see Discussion). Taken together, we found that vSUB PV transcriptomes exhibit striking differences in isoform expression among the three *Nrxns*, but do not display sex-dependent differences in *Nrxn* expression profiles. It is possible that the sex-specific effects of PV-*Nrxn3* KO are driven by other elements of the synaptic environment that influence, or are influenced by, *Nrxn3* signaling. These may include sex-specific expression or localization of post-synaptic adhesion molecules or sex- and cell-type-specific initiation of different intracellular signaling pathways in PV or RS/BS neurons.

As a step toward exploring possible cell-type- and sex-specific ligand localization, we investigated the localization of two prototypical Nrnx ligands that influence inhibitory synaptic transmission, neuroligin-2 and neuroligin-3 (Nlgn2 and Nlgn3). Nlgn2 is exclusively localized to inhibitory synapses while Nlgn3 is localized to excitatory and inhibitory synapses. We filled RS and BS neurons in *ex vivo* vSUB slices with biocytin, then re-sectioned these slices and performed quadruple fluorescent immunohistochemistry (IHC) (Figures S6A and S6B). We found that co-localization of presynaptic PV with postsynaptic Nlgn2 or with Nlgn3 does not differ between RS and BS principal neurons in male or female vSUB (Figures S6C and S6D). To test whether the data reflect co-localization between PV-Nlgn2 and PV-Nlgn3 immunoreactive puncta or represent analysis artifacts due to chance overlap with nearby PV-negative GABAergic synapses, we reflected the PV channel along the x- and y-axes (shuffled) and reanalyzed the data. If artifacts drove the co-localization values, we would anticipate that the actual and shuffled data should be similar; however, we observed that the co-localization in the shuffled dataset was reduced for all cells (Hoon et al., 2009; Liu et al., 2018; Figures S6C and S6D). These data indicate that differential localization of Nlgn2 and Nlgn3 is likely not responsible for the differences in PV-mediated synaptic strength on RS and BS neurons.

DISCUSSION

Despite decades of intense scrutiny, fundamental insight into the distinct and non-overlapping functions of individual Nrnxn at inhibitory synapses remains elusive. Based on studies from excitatory synapses, there is growing support for the notion that individual Nrnxn can participate in non-redundant roles at the same synapse as well as distinct roles at different synapses (Aoto et al., 2015; Dai et al., 2019, 2021). A common yet untested assumption is that the usage of Nrnxn at synapses is independent of sex. Here, we utilized *in vivo* manipulations of Nrnx3 coupled with cell-type- and synapse-specific morphological and electrophysiological analyses and considered sex as a biological variable to ask whether Nrnx3 performs a functionally essential role at inhibitory synapses in vSUB. The findings we report herein support three unexpected and significantly important conclusions that may cause us to revise how we view the functional organization of local circuits and usage of Nrnxn.

First, although local vSUB circuit dysfunction has been implicated in disease, a cell-type-specific understanding of this circuit is limited. Additionally, consistent with most microcircuit dissections in other brain regions, characterization of the vSUB local circuit has only used male animals. Here, we reveal that RS and BS principal neurons receive different relative levels of PV inhibition, but that this functional organization is sexually dimorphic. In female vSUB, PV interneurons display stronger evoked inhibition onto BS principal neurons. In male vSUB we observe the opposite—PV interneurons provide greater inhibition to RS neurons. The most parsimonious explanation of these sex differences is that they are driven by a common mechanism; however, we discovered that the degree of PV-mediated inhibition is governed by distinct synaptic properties: differences in postsynaptic strength in females, but synapse numbers in males, drive asymmetric PV inhibition. The sexually dimorphic and cell-type-specific organization of the vSUB microcircuit provides

support to the notion that information gleaned from circuit-level studies in male rodents might not always be directly transposable between sexes.

Second, the investigation of Nrnx3 has historically not considered sex as a biological variable. This has led to the assumption that Nrnx3 functions in neurons from male and female rodents are superimposable. Here, we tested this assumption and provide evidence that Nrnx3 usage can be sexually dimorphic. Conditional deletion of Nrnx3 from PV interneurons resulted in striking sex-dependent synaptic phenotypes at subicular PV-RS synapses. Our data suggest that at PV-RS synapses, Nrnx3 serves to suppress presynaptic release in females, but promote postsynaptic strength and synapse maintenance in males. The finding that Nrnx3 can function to suppress neurotransmitter release has not been previously reported and serves to expand our functional understanding of these enigmatic molecules.

Is Nrnx3 the arbiter responsible for shaping the connectivity biases we observe in vSUB? In males, we demonstrate that Nrnx3 is required for establishing connectivity bias by promoting PV-RS synapse numbers (Figure 6G). In females, however, post-synaptic strength is greater onto BS neurons, which is not mediated by Nrnx3 (Figure 6B). Instead, PV-Nrnx3 KO revealed that Nrnx3 contributes to asymmetric PV-mediated inhibition in female vSUB by suppressing PV-RS release probability (Figure 5E). Thus, it appears there may be other factors that dictate post-synaptic strength at PV-BS synapses in females. These factors could originate at the pre- or post-synapse. Our scRNA-seq revealed six protein-coding genes that are upregulated in male compared to female vSUB PV neurons, that is, *Ddx3y*, *Eif2s3y*, *Vip*, *Penk*, *Dkk3*, and *Plp1*, and one gene upregulated in female PVs, *Gstm1* (Figures 7G and 7H). *Ddx3y* (DEAD-box helicase 3y) and *Eif2s3y* (eukaryotic translation initiation factor) are Y-linked genes involved in translation and may contribute to neuronal differentiation (*Ddx3y*) and synaptic transmission (*Eif2s3y*; Zhang et al., 2021) in male mice. The secreted glycoprotein *Dkk3* (Dickkopf-3) is a negative modulator of Wnt signaling and may play a role in neuron differentiation in development and have a neuroprotective role after development (Busceti et al., 2018). *Gstm1* (glutathione-S-transferase mu 1) is neuroprotective against oxidative stress (Kumar et al., 2017). *Plp1* encodes for proteolipid protein and DM20. In neurons, PLP is soma restricted and may play a role in vesicular transport (Jacobs et al., 2003). *Penk* and *Vip* encode for proenkephalin and vasoactive intestinal peptide, respectively, and are neuromodulatory peptides that are not typically found in medial ganglionic eminence-derived hippocampal interneurons such as PV neurons, but more commonly identified in interneurons derived from the caudal ganglionic eminence (Harris et al., 2018; Lukacsovich et al., 2019). Their high expression in male fast-spiking, *Lhx6*⁺ and *PV*⁺ vSUB neurons (Figure S5) is curious and merits further evaluation. Whether the expression of these seven genes contribute to the sex-specific PV synaptic transmission in vSUB will be of interest to investigate in future studies.

Third, we report that Nrnx3 expressed in the same presynaptic cell type can, dependent on postsynaptic cell identity, differentially govern aspects of inhibitory synapse function. In both male and female vSUB, genetic ablation of Nrnx3 in PV-positive interneurons resulted in altered inhibition onto RS principal neurons but appeared to be rather dispensable at PV-BS synapses. How can the differential usage of Nrnx3 by PV neurons be explained?

Given that scRNA-seq of PV neurons did not reveal sex-specific differences in Nrnx3 mRNA levels, two appealing and non-mutually exclusive possibilities could involve (1) directed localization of Nrnx3 α primarily to PV-RS synapses and/or (2) differential protein expression/localization of inhibitory postsynaptic ligands (e.g., neuroligin-2 or neuroligin-3, GABA_ARs, cerebellins/GluD1, dystroglycan [Lévi et al., 2002; Südhof, 2017]) or other synaptic molecules at vSUB PV synapses. Here, we indicate that localization of two prototypical Nrnx ligands, Nlgn2 and Nlgn3, at PV synapses do not display cell-type-specific differences (Figure S6). Our findings suggest that an individual Nrnx may not always govern a generalizable function at all synapses made by the same presynaptic neuron and may have broad implications when investigating the circuit-level role of Nrnxns.

While sex differences in neuromodulation at inhibitory synapses have been described in hippocampus (Huang and Woolley, 2012; Tabatadze et al., 2015), our findings indicate a sex-specific basal *intrinsic connectivity* bias. Here, we did not assess variation in circulating gonadal hormone levels among experimental animals. While circulating hormones may play a role in the sex-specific inhibition, it is important to note that the variance in IPSC amplitudes was not significantly different between females and males, suggesting that any hormonal fluctuations among individual animals was not a significant contributing factor mediating the robust phenotypes we observed.

The asymmetric inhibitory control of RS/BS by PVs could facilitate differential engagement of local subiculum and downstream brain regions during specific behaviors. Accordingly, RS and BS neurons are differentially engaged during *in vivo* sharp-wave ripple activity in males, suggesting that inhibitory connectivity bias confers physiological relevance during memory consolidation (Böhm et al., 2015; Maslarova et al., 2015). The sex differences in PV connectivity and Nrnx3 usage are particularly intriguing in the context of neuropsychiatric disorders. Mutations in *NRXN3* may contribute to sex-specific symptoms by differentially altering vSUB activity in males versus females. Further studies to investigate whether vSUB microcircuit connectivity or output is altered sex specifically in neuropsychiatric disorders would elucidate disease mechanisms and aid therapeutic development. Additionally, it is important to determine whether the sex-dependent organization and usage of Nrnxns is a generalizable feature of all microcircuits or specific to a subset of local circuits.

Limitations of the study

While our data demonstrate distinct sex- and cell-type-specific roles for Nrnx3 in governing PV-mediated inhibition in vSUB, our scRNA-seq results did not reveal differences in Nrnx3 mRNA levels in male and female PV neurons. Measurements of Nrnx expression have relied heavily on quantitative mRNA approaches because antibodies to individual Nrnx isoforms are not reliable (Südhof, 2017). Thus, we cannot test whether the Nrnx3 protein produced in PV neurons is equally distributed to all synapses or whether it displays preferential trafficking to PV-RS synapses to govern synaptic properties or whether the presynaptic localization of Nrnx3 is identical in male and female PV neurons. Differences in Nrnx3 localization may in fact help explain the cell-type- and sex-specific PV-Nrnx3 KO phenotype. To circumvent the lack of reliable isoform-specific antibodies, epitope-tagged

Nrxn1 mice have been generated and have been used to investigate Nrxn1 trafficking (Ribeiro et al., 2019) and sub-synaptic localization at excitatory synapses (Trotter et al., 2019). However, approaches to investigate the endogenous protein levels of Nrxn3 are currently undeveloped.

Similar limitations hinder our ability to examine postsynaptic ligand usage at PV-RS and PV-BS synapses. While scRNA-seq of RS and BS neurons harvested from female and male vSUB may identify differentially expressed mRNAs encoding for inhibitory Nrxn ligands or synaptic proteins, the interpretation regarding how identified mRNAs function at PV-pyramidal synapses is not straightforward. Although the full diversity of GABAergic neurons in vSUB is uncharacterized, it is likely that inhibitory synapses on principal neurons in vSUB exhibit profound molecular and functional heterogeneity similar to that observed in hippocampus proper. Therefore, differences in mRNA levels of postsynaptic proteins cannot be directly attributable to PV-RS or PV-BS synapse function. In line with this logic, postsynaptic proteins that contribute to the cell type and sex differences observed in the present study need not be differentially expressed at the mRNA level but might be regulated via protein trafficking. Indeed, functional and morphological studies suggest that Nrxn ligands can exhibit differential trafficking to inhibitory synapses (Földy et al., 2013; Gibson et al., 2009; Uchigashima et al., 2020; Zhang et al., 2015). Regardless of mRNA levels, two questions need to be addressed in order to validate putative candidate proteins that may contribute to the PV-Nrxn3 KO phenotypes: (1) Is the protein trafficked to PV-pyramidal synapses? and (2) Does ablation of the postsynaptic protein selectively recapitulate the PV-Nrxn3 KO phenotype at PV-RS synapses? To accurately address these questions, validated commercial antibodies and conditional knockout mice are required.

STAR★METHODS

RESOURCE AVAILABILITY

Lead contact—Further information and requests for resources and reagents should be directed to and will be fulfilled by the lead contact, Jason Aoto (jason.aoto@cuanschutz.edu).

Materials availability—Plasmids generated in this study are available upon request.

Data and code availability

- Single-cell RNA-seq data have been deposited at GEO and are publicly available as of the date of publication. Accession number is listed in the key resources table.
- All original code has been deposited at Zenodo and is publicly available as of the date of publication. DOI is listed in the key resources table.
- Any additional information required to reanalyze the data reported in this paper is available from the lead contact upon request.

EXPERIMENTAL MODEL AND SUBJECT DETAILS

Mice were bred at the University of Colorado Anschutz and were from a B6;129 or B6.Cg mixed genetic background. Pvalb^{tm1(cre)Arbr/J} homozygote mice (“PV-IRES-Cre,” Jax 008069) breeders were kindly provided by Dr. Diego Restrepo and *Nrxn3^{tm3Sud/J}* (“Nrxn3 cKO,” Jax 014157) breeders were a generous gift from Dr. Thomas Südhof. Gt(ROSA)26Sortm9(CAG-tdTomato)Hze/J (“Ai9”: Jax 007909) mice were obtained from The Jackson Laboratory. Mice were housed in a dedicated animal care facility maintained at 35% humidity, 21–23°C, on a 14/10 light/dark cycle. Mice were housed in groups of 2–5 in ventilated cages with same-sex littermates with food and water *ad libitum*. Mice were genotyped in-house, and sex of the animal was determined by external genitalia. Animals were randomly selected for experiments. Animals were stereotactically injected at P21–22, and all other experiments were performed at P35–42 in visibly healthy animals. All procedures were conducted in accordance with guidelines approved by Administrative Panel on Laboratory Animal Care at University of Colorado, Anschutz School of Medicine, accredited by Association for Assessment and Accreditation of Laboratory Animal Care International (AAALAC) (00235).

METHOD DETAILS

Stereotactic viral injections—Stereotactic injections were performed on P21–22 mice. Animals were anesthetized with an intraperitoneal injection of 2,2,2-Tribromoethanol (250 mg/kg) then head fixed to a stereotactic frame (KOPF). After drilling small holes in the skull using a handheld drill, 0.5–1.0 μ L solutions of adeno associated viruses (AAVs) were injected with pulled glass micropipettes into ventral subiculum at a rate of 11–14 μ L/hr using a syringe pump (World Precision Instruments). Coordinates (in mm) were: rostrocaudal: –3.1, mediolateral: +/- 3.2 (relative to Bregma), and dorsoventral: –3.3 (relative to pia). All AAVs used in this study were packaged in-house: AAV DJ-hSYN-DIO_{loxP}-ChIEF-mRuby, AAV DJ-hSYN-DIO_{loxP}-mGFP-T2A-Synaptophysin-mRuby, AAV DJ-hSYN-DIO_{loxP}-mRuby, as previously described (Aoto et al., 2013). AAV vectors were constructed from an empty cloning vector where the expression cassette is as follows: left-ITR of AAV2, human synapsin promoter, 5' LoxP site, multiple cloning site, 3' LoxP site and right ITR. AAV plasmids were co-transfected with pHelper and pRC-DJ into HEK293T cells. 72 hr post transfection, cells were harvested and lysed and virus harvested from the 40% iodixanol fraction. Virus was concentrated in a 100K MWCO ultracon filter.

Ex vivo whole-cell electrophysiology—At P35–P42, animals were deeply anesthetized with isoflurane and decapitated. Brains were rapidly dissected and 300 μ m horizontal slices were sectioned with a vibratome (Leica VT1200) in ice cold high-sucrose cutting solution containing (in mM) 85 NaCl, 75 sucrose, 25 D-glucose, 24 NaHCO₃, 4 MgCl₂, 2.5 KCl, 1.3 NaH₂PO₄, and 0.5 CaCl₂. Slices were transferred to 31.5°C oxygenated ACSF containing (in mM) 126 NaCl, 26.2 NaHCO₃, 11 D-Glucose, 2.5 KCl, 2.5 CaCl₂, 1.3 MgSO₄·7H₂O, and 1 NaH₂PO₄ for 30 min, then recovered at room temperature for at least 1 hour before recordings. During recordings, slices were superfused with 29.5°C ACSF containing 10 μ M NBQX and 50 μ M D-AP5 to isolate GABAergic currents, unless otherwise indicated. For strontium experiments, CaCl₂ was replaced with 2.5mM SrCl₂ in the ACSF. Pyramidal neurons in subiculum were visually identified with an Olympus BX51W microscope with a

40x dipping objective collected on a Hamamatsu ORCA-Flash 4.0 V3 digital camera using an IR bandpass filter. Neurons were voltage-clamped at -70 mV in whole-cell configuration with a high-chloride internal solution containing (in mM) 95 K-gluconate, 50 KCl, 10 HEPES, 10 Phosphocreatine, 4 Mg_2 -ATP, 0.5 Na_2 -GTP, and 0.2 EGTA.

To determine pyramidal neuron identity (regular versus burst spiking), neurons were current-clamped and injected with 500ms depolarizing current in 50 pA steps: cells that fired bursts upon suprathreshold current injection (2–4 spikes with ~ 10 ms inter-spike interval) were classified as burst spiking whereas those that did not fire bursts were classified as regular spiking. To optogenetically stimulate ChIEF expressing PVs, slices were illuminated with 470 nm LED light (ThorLabs M470L2-C1) for 3 ms through the 40x dipping objective located directly over the recorded cell. With an illumination area of 33.18mm^2 the tissue was excited with an irradiance of 0.006 to 0.17 mW/mm^2 . All recordings were acquired using Molecular Devices Multiclamp 700B amplifier and Digidata 1440 digitizer with Axon pClamp™ 9.0 Clampex software, lowpass filtered at 2 kHz and digitized at 10–20 kHz.

Analysis of electrophysiology recordings—Evoked IPSC peak amplitudes from each recording were identified using Axon™ pClamp10 Clampfit software or MATLAB (Mathworks, Inc) using custom scripts. To obtain input/output curves, 12–15 sweeps (0.1 Hz) were averaged to obtain peak amplitude at each stimulus intensity. All final IPSC values are displayed as the absolute value. Input/output slope was calculated using the SLOPE function in Microsoft Excel: (amplitude range/intensity range). In optogenetic experiments, PV-IPSC amplitudes often began to plateau when large light input-intensities were reached. Thus, slope was calculated from linear regions of the curves, which encompassed the first three points (0.2–1.8 mW).

Release probability was assessed by measurements of paired-pulse ratios (PPRs) at inter-stimulus intervals of 25–55 ms. PPR was measured by dividing the average IPSC amplitude evoked by the second stimulus by the average IPSC amplitude evoked by the first stimulus (R_2/R_1). For strontium experiments, slices were illuminated at 0.25 Hz 7 times. The amplitudes of asynchronous IPSC events that occurred within a 300 ms window immediately following the phasic IPSC (which occurs due to residual calcium) were analyzed using Clampfit event detection software. For analysis of IPSC kinetics, IPSC sweeps were averaged per cell, and rise time and decay tau were calculated using Clampfit functions. Rise time was calculated from the middle 20%–80% of the rise slope. Decay time constant values and weights were calculated by fitting the decay slope to a standard, two-term exponential function, fitted with Levenberg-Marquardt method. Weighted decay tau was calculated as $T_w = ((T_1 * A_1) + (T_2 * A_2)) / (A_1 + A_2)$.

Synaptically connected paired recordings—Paired recordings were made from slices prepared in conditions described above; ACSF contained 10 μM NBQX and 50 μM D-AP5 and high chloride internal was used. PV neurons were visualized using PV-Cre x Ai9 transgenic animals (Td+ neurons) or by injecting AAV-DIO-mRuby into vSUB of PV-Cre or PV-Cre x $Nrxn3^{fl/fl}$ animals (mRuby+ neurons). PV neurons and nearby RS or BS neurons were patched in whole-cell configuration, then PV neurons were stimulated with 5 ms of 800 pA current in current-clamp to elicit single action potentials while simultaneously

recording the RS or BS cell in voltage-clamp. If the PV spike caused a unitary IPSC (uIPSC) in the RS/BS cell (> 10 pA deflection from baseline), the pair was considered connected. uIPSC amplitude was calculated from the mean peak amplitude of 20 sweeps (0.1 Hz). Connectivity rate was calculated as synaptically connected PV-RS or PV-BS pairs divided by the total PV-RS or PV-BS pairs tested per animal, respectively. Animals from which neither PV-RS nor PV-BS connected pairs were achieved were excluded from the calculation. Thus, for a situation in which 0/5 PV-RS and 4/5 PV-BS pairs were connected from one animal, both values would be utilized in the calculation of the mean connectivity rate, but for a situation where 0/5 PV-RS and 0/5 PV-BS pairs were connected, neither value would be used for connectivity analysis.

PV neuron excitability and density—To measure vSUB PV neuron resting membrane and intrinsic firing properties (Figure 2), acute slices were made from PV-Cre x Ai9 mice and TdTomato+ cells were patched in whole-cell configuration using an internal solution containing (in mM) 140 K-gluconate, 5 KCl, 10 HEPES, 10 Phosphocreatine, 4 Mg₂-ATP, 0.5 Na₂-GTP, and 0.2 EGTA. The ACSF contained 100 μ M picrotoxin to isolate spontaneous EPSCs. Cells were first voltage-clamped at -70 to measure EPSCs and resting membrane properties, then current-clamped and given -150 to $+400$ pA current injections in 25 pA steps. Action potential phase plots, half-width and amplitude were calculated from spikes at rheobase. Sag was calculated as the ratio of the steady state voltage to the maximum decrease in voltage following -150 pA current injection for 500 ms.

To quantify PV cell density in vSUB, PV-Cre x Ai9 mice were transcardially perfused with cold 0.01 M PBS followed by 4% PFA. The brain was fixed in 4% PFA for 2 hours then transferred to a 30% sucrose 4% PFA solution overnight at 4°C. The following day the brain was embedded in OCT compound, rapidly frozen on dry ice, then horizontally cryo-sectioned into 30 μ m thick slices. Slices were coverslipped with DAPI fluoromount then imaged with an Olympus VS120 slide scanning microscope. To quantify PV neuron density, an ROI was drawn around vSUB and TdTomato+ PV cell somas were counted and normalized to ROI area using MATLAB.

PV synapse imaging—To determine PV synapse density among RS/BS neurons, PV-Cre or PV-Nrxn3 KO mice were injected with AAV-hSYN-DIO-mGFP-T2A-Synaptophysin-mRuby into vSUB and 300 μ m acute slices were made 14–21 days later. vSUB pyramidal neurons were patched with an internal solution containing biocytin for 15 minutes and fired to determine neuron identity. Slices were then fixed in 4% PFA overnight at 4°C, washed in PBS, then incubated with Jackson Immunoresearch CyTM5-conjugated Streptavidin (1:500) in PBS with 0.2% Triton-X for 48 hours at 4°C. Slices were washed and coverslipped then filled cells were imaged on a 3I Marinas spinning disk confocal microscope using a 63x oil objective and z-steps of 0.27–0.5 μ m. Images of filled cells were background subtracted, 3D reconstructed and quantified using MATLAB with *DIPimage* toolbox and using custom written routines. Somatic and perisomatic PV synapses were identified as mRuby+, GFP+ puncta that overlapped with Cy-5 signal in the ROI drawn around soma and a -10 μ m section of apical dendrite. To account for overlapping synapses, total PV synaptic volume

colocalized with each RS/BS soma was calculated and normalized to the soma volume as an estimate of synapse density per cell.

Neuroigin-2 and -3 immunohistochemistry—To quantify co-localization of neuroligin ligands with PV synapses made onto RS and BS neurons, RS/BS cells were filled in 300 μm slices as described above then resectioned and immunohistochemistry was performed to simultaneously detect parvalbumin, Neuroigin 2 (Nlgn2) and Neuroigin 3 (Nlgn3), as follows. Slices containing filled cells were fixed in 4% PFA for 3 hours at 4°C, then transferred to 30% sucrose in PBS overnight at 4°C. Slices were resectioned the following day into 30 μm -thick sections using a cryostat and immediately processed in 24-well plates in the following steps: 1) four 15 minute PBS washes, 2) 1 hour incubation at room temperature in blocking solution (5% normal donkey serum, 0.3% Triton X, 0.02% Sodium Azide in PBS), 3) incubation at 4°C with primary antibodies in blocking solution for 16–20 hours, 4) three 15 minute PBS washes, 5) incubation at room temperature with secondary antibodies in blocking solution (protected from light), 6) three 15 minute PBS washes. The primary antibody incubation included: DyLight 405-conjugated streptavidin (1:300), Immunostar guinea pig parvalbumin antibody (1:5,000), SySy Neuroigin-2 mouse antibody (2 $\mu\text{g}/\text{mL}$), and Neuroigin-3 rabbit antibody (1:500) (generous gift from Dr. Peter Scheiffele; Budreck and Scheiffele, 2007). The secondary antibody incubation included: donkey anti-guinea pig Cy2 (1:200), donkey anti-mouse Cy3 (1:200), donkey anti-rabbit AlexaFluor 647 (1:200), and DyLight 405 streptavidin (1:500). Stained slices were mounted onto slides and coverslipped, then filled cells were imaged on a 3I Marinas spinning disk confocal microscope with a 63x oil objective using 0.27 μm z-steps.

The density of colocalized PV-Nlgn2 and PV-Nlgn3 puncta on RS/BS 405+ somas was quantified in ImageJ using the DiAna plugin for each individual section of a Z stack that contained a 405-positive soma (Gilles et al., 2017). Images were processed using DiAna prior to analysis. Briefly, an optimal high-pass threshold was determined for each stack, which was then applied to all sections. Images where thresholding failed to delineate individual puncta across all sections were excluded from the final analysis. To verify PV-Nlgn2 and PV-Nlgn3 colocalization was not due to analysis artifact (random overlap with nearby signal), the PV-488 channel was reflected along the x- and y- axes to shuffle PV puncta and colocalization was quantified again.

Single-cell mRNA sequencing—Single-cell mRNA was collected from PV neurons as follows. The work area was wiped down with RNase Away before cell collection. PV cells in vSUB slices were patched in whole-cell configuration using < 1 μL of internal solution, fired to confirm fast-spiking identity, and aspirated. Cells were expelled into PCR tubes containing cold lysis buffer and RNase inhibitor, spun briefly, then snap-frozen on dry ice and stored at -80°C until further processing with the Takara SMART-Seq HT kit, performed according to the manufacturer's protocol. One-step RTPCR was performed using poly-A selection, eliminating the possibility of genomic contamination. Resulting single-cell cDNA was purified and subsequently analyzed on a Fragment Analyzer (Advanced Analytical) to determine concentration and assess sample quality. Library preparation was performed using Nextera XT DNA Library Preparation Kit (Illumina) then sequenced in an

Illumina NovaSeq6000 instrument (150 bp, paired-end). Sequencing data were aligned using STAR aligner with the following parameters: trim_front1 = 10, cut_front_mean_quality = 20, average_quality = 0, length_required = 30. The quantification was performed with FeatureCounts. EdgeR (Bioconductor) was used to normalize for equal library size across samples using the trimmed means of the M-values normalization method (producing a single-cell gene expression factor for each cell), then differential gene expression analysis was performed.

For neurexin isoform level analysis, a modified lasso regression was used to determine the fraction of reads per each exon. Each gene (Nrxn 1–3) was defined by two or three major isoforms: alpha, beta, and gamma, as established in prior literature. An extra factor was allowed for, where each gene had a probability of being expressed (depending on the sex and exon), representing exon dropout, and a penalty factor was added for low p values. Finally, a decay rate factor was added to account for the potential loss in alignment fidelity farther from the end of an isoform. The predicted isoform expression level was then normalized to its single-cell gene expression factor. For alternative splicing analysis, the number of reads that fell on splice junctions were quantified: for each cell, counts of exon inclusion (splice-in) and exon exclusion (splice-out) were added per junction. The mean and SEM for each value, within each sex, was then calculated and normalized such that the two means added to one.

QUANTIFICATION AND STATISTICAL ANALYSIS

All statistical analysis was performed in Prism 7 (GraphPad) with the exception of strontium cumulative probability plots and single-cell RNA sequencing data. Data were tested for normality using D'Agostino & Pearson normality tests, then Student's unpaired two-tailed t tests, ANOVAs, or Welch tests (RNA sequencing data) were used to assess differences between groups in normally distributed datasets. If data did not exhibit normal distribution, they were assessed using Mann-Whitney or Kruskal-Wallis tests. Male/female Nrxn RNA isoform expression levels were compared using Welch's t test. Strontium cumulative probability plots were compared using Kolmogorov-Smirnoff tests on AAT Bioquest (aatbio.com). RNA sequencing analysis was performed using edgeR (Bioconductor) and Python. Basal sex differences in PV inhibition (Figures 1 and 3) were determined by analyzing control animals separately from the PV-Nrxn3 KO experiments (Figures 4 and 6) and were presented separately to facilitate clarity and comprehension. All experiments were replicated in at least 3 animals (per condition, per sex). Experimenter was not blinded to animal sex, genotype, or cell identity during data acquisition, but was blinded during image analysis, RNA sequencing analysis, and most electrophysiological analysis. Cells of poor quality were excluded from electrophysiology analysis (i.e., unstable/noisy baseline, access resistance > 10% of membrane resistance) and from RNA sequencing (4/58 cells did not pass initial quality control assessments, i.e., cells with library size and expressed gene counts that are three median absolute deviation smaller than the median of library size and median of expressed gene counts from all cells, respectively). Statistical tests used for each experiment and exact p values are located in figure legends. Differences were considered statistically significant if $p < 0.05$. In figures, * $p < 0.05$, ** $p < 0.01$, *** $p < 0.001$, and **** $p < 0.0001$, ^{ns} $p > 0.05$. Sample sizes can be found within figures or in figure legends

and are notated: n/N = cell or pair number / animal number. Average values are expressed as arithmetic mean \pm SEM.

Supplementary Material

Refer to Web version on PubMed Central for supplementary material.

ACKNOWLEDGMENTS

We thank members of the Aoto Lab for thoughtful discussions. We thank Dr. Kevin Beier for the generous gift of the synaptophysin-mRuby plasmid and Dr. Peter Scheiffele for the generous gift of the rabbit anti-Nlgn3 antibody. This work was supported by grants from the NIH (R00MH103531 and R01MH116901 to J.A., R35NS116879 to M.J.K., and T32NS099042 and 1F31MH125510 to E.E.B.), the Brain & Behavior Research Foundation (NARSAD24847 to J.A.), and the Swiss National Science Foundation (Switzerland, CRETP3_166815 to C.F.).

REFERENCES

- Aoto J, Martinelli DC, Malenka RC, Tabuchi K, and Südhof TC (2013). Presynaptic neuroligin-3 alternative splicing trans-synaptically controls post-synaptic AMPA receptor trafficking. *Cell* 154, 75–88. [PubMed: 23827676]
- Aoto J, Földy C, Ilcus SMC, Tabuchi K, and Südhof TC (2015). Distinct circuit-dependent functions of presynaptic neuroligin-3 at GABAergic and glutamatergic synapses. *Nat. Neurosci* 18, 997–1007. [PubMed: 26030848]
- Bartos M, and Elgueta C (2012). Functional characteristics of parvalbumin- and cholecystokinin-expressing basket cells. *J. Physiol* 590, 669–681. [PubMed: 22250212]
- Becker JB (2016). Sex differences in addiction. *Dialogues Clin. Neurosci* 18, 395–402. [PubMed: 28179811]
- Beier KT, Steinberg EE, DeLoach KE, Xie S, Miyamichi K, Schwarz L, Gao XJ, Kremer EJ, Malenka RC, and Luo L (2015). Circuit architecture of VTA dopamine neurons revealed by systematic input-output mapping. *Cell* 162, 622–634. [PubMed: 26232228]
- Bekkers JM, and Clements JD (1999). Quantal amplitude and quantal variance of strontium-induced asynchronous EPSCs in rat dentate granule neurons. *J. Physiol* 516, 227–248. [PubMed: 10066937]
- Böhm C, Peng Y, Maier N, Winterer J, Poulet JFA, Geiger JRP, and Schmitz D (2015). Functional diversity of subicular principal cells during hippocampal ripples. *J. Neurosci* 35, 13608–13618. [PubMed: 26446215]
- Böhm C, Peng Y, Geiger JRP, and Schmitz D (2018). Routes to, from and within the subiculum. *Cell Tissue Res.* 373, 557–563. [PubMed: 29808383]
- Brown SM, Clapcote SJ, Millar JK, Torrance HS, Anderson SM, Walker R, Rampino A, Roder JC, Thomson PA, Porteous DJ, and Evans KL (2011). Synaptic modulators *Nrxn1* and *Nrxn3* are dysregulated in a *Disc1* mouse model of schizophrenia. *Mol. Psychiatry* 16, 585–587. [PubMed: 21321563]
- Budreck EC, and Scheiffele P (2007). Neuroligin-3 is a neuronal adhesion protein at GABAergic and glutamatergic synapses. *Eur. J. Neurosci* 26, 1738–1748. [PubMed: 17897391]
- Busceti CL, Di Menna L, Bianchi F, Mastroiacovo F, Di Pietro P, Traficante A, Bozza G, Niehrs C, Battaglia G, Bruno V, et al. (2018). Dickkopf-3 causes neuroprotection by inducing vascular endothelial growth factor. *Front. Cell. Neurosci* 12, 292. [PubMed: 30258353]
- Cembrowski MS, Phillips MG, DiLisio SF, Shields BC, Winnubst J, Chandrashekar J, Bas E, and Spruston N (2018). Dissociable structural and functional hippocampal outputs via distinct subiculum cell classes. *Cell* 173, 1280–1292.e18. [PubMed: 29681453]
- Dai J, Aoto J, and Südhof TC (2019). Alternative splicing of presynaptic neuroligins differentially controls postsynaptic NMDA and AMPA receptor responses. *Neuron* 102, 993–1008.e5. [PubMed: 31005376]
- Dai J, Patzke C, Liakath-Ali K, Seigneur E, and Südhof TC (2021). GluD1 is a signal transduction device disguised as an ionotropic receptor. *Nature* 595, 261–265. [PubMed: 34135511]

- Földy C, Malenka RC, and Südhof TC (2013). Autism-associated neuroligin-3 mutations commonly disrupt tonic endocannabinoid signaling. *Neuron* 78, 498–509. [PubMed: 23583622]
- Földy C, Darmanis S, Aoto J, Malenka RC, Quake SR, and Südhof TC (2016). Single-cell RNAseq reveals cell adhesion molecule profiles in electrophysiologically defined neurons. *Proc. Natl. Acad. Sci. USA* 113, E5222–E5231. [PubMed: 27531958]
- Freire-Cobo C, and Wang J (2020). Dietary phytochemicals modulate experience-dependent changes in Neurexin gene expression and alternative splicing in mice after chronic variable stress exposure. *Eur. J. Pharmacol* 883, 173362. [PubMed: 32663544]
- Fuccillo MV, Földy C, Gökce Ö, Rothwell PE, Sun GL, Malenka RC, and Südhof TC (2015). Single-cell mRNA profiling reveals cell-type-specific expression of neurexin isoforms. *Neuron* 87, 326–340. [PubMed: 26182417]
- Gibson JR, Huber KM, and Südhof TC (2009). Neuroligin-2 deletion selectively decreases inhibitory synaptic transmission originating from fast-spiking but not from somatostatin-positive interneurons. *J. Neurosci* 29, 13883–13897. [PubMed: 19889999]
- Gill KM, and Grace AA (2014). Corresponding decrease in neuronal markers signals progressive parvalbumin neuron loss in MAM schizophrenia model. *Int. J. Neuropsychopharmacol* 17, 1609–1619. [PubMed: 24787547]
- Gilles J-F, Dos Santos M, Boudier T, Bolte S, and Heck N (2017). DiAna, an ImageJ tool for object-based 3D co-localization and distance analysis. *Methods* 115, 55–64. [PubMed: 27890650]
- Grace AA (2010). Dopamine system dysregulation by the ventral subiculum as the common pathophysiological basis for schizophrenia psychosis, psychostimulant abuse, and stress. *Neurotox. Res* 18, 367–376. [PubMed: 20143199]
- Graves AR, Moore SJ, Bloss EB, Mensh BD, Kath WL, and Spruston N (2012). Hippocampal pyramidal neurons comprise two distinct cell types that are countermodulated by metabotropic receptors. *Neuron* 76, 776–789. [PubMed: 23177962]
- Harris E, Witter MP, Weinstein G, and Stewart M (2001). Intrinsic connectivity of the rat subiculum: I. Dendritic morphology and patterns of axonal arborization by pyramidal neurons. *J. Comp. Neurol* 435, 490–505. [PubMed: 11406828]
- Harris KD, Hochgerner H, Skene NG, Magno L, Katona L, Bengtsson Gonzales C, Somogyi P, Kessaris N, Linnarsson S, and Hjerling-Leffler J (2018). Classes and continua of hippocampal CA1 inhibitory neurons revealed by single-cell transcriptomics. *PLoS Biol.* 16, e2006387. [PubMed: 29912866]
- Hishimoto A, Liu Q-R, Drgon T, Pletnikova O, Walther D, Zhu X-G, Troncoso JC, and Uhl GR (2007). Neurexin 3 polymorphisms are associated with alcohol dependence and altered expression of specific isoforms. *Hum. Mol. Genet* 16, 2880–2891. [PubMed: 17804423]
- Hoffman GE, Ma Y, Montgomery KS, Bendl J, Jaiswal MK, Kozlenkov A, Peters MA, Dracheva S, Fullard JF, Chess A, et al. (2021). Sex differences in the human brain transcriptome of cases with schizophrenia. *Biol. Psychiatry*, Published March 25, 2021. 10.1016/j.biopsych.2021.03.020.
- Hoon M, Bauer G, Fritschy J-M, Moser T, Falkenburger BH, and Varoqueaux F (2009). Neuroligin 2 controls the maturation of GABAergic synapses and information processing in the retina. *J. Neurosci* 29, 8039–8050. [PubMed: 19553444]
- Huang GZ, and Woolley CS (2012). Estradiol acutely suppresses inhibition in the hippocampus through a sex-specific endocannabinoid and mGluR-dependent mechanism. *Neuron* 74, 801–808. [PubMed: 22681685]
- Jacobs EC, Bongarzone ER, Campagnoni CW, Kampf K, and Campagnoni AT (2003). Soma-restricted products of the myelin proteolipid gene are expressed primarily in neurons in the developing mouse nervous system. *Dev. Neurosci* 25, 96–104. [PubMed: 12966208]
- Kelai S, Maussion G, Noble F, Boni C, Ramoz N, Moalic J-M, Peuchmaur M, Gorwood P, and Simonneau M (2008). *Nrxn3* upregulation in the globus pallidus of mice developing cocaine addiction. *Neuroreport* 19, 751–755. [PubMed: 18418251]
- Kim Y, and Spruston N (2012). Target-specific output patterns are predicted by the distribution of regular-spiking and bursting pyramidal neurons in the subiculum. *Hippocampus* 22, 693–706. [PubMed: 21538658]

- Koehnke J, Katsamba PS, Ahlsen G, Bahna F, Vendome J, Honig B, Shapiro L, and Jin X (2010). Splice form dependence of β -neurexin/neurologin binding interactions. *Neuron* 67, 61–74. [PubMed: 20624592]
- Konradi C, Yang CK, Zimmerman EI, Lohmann KM, Gresch P, Pantazopoulos H, Berretta S, and Heckers S (2011). Hippocampal interneurons are abnormal in schizophrenia. *Schizophr. Res* 131, 165–173. [PubMed: 21745723]
- Kumar A, Dhull DK, Gupta V, Channana P, Singh A, Bhardwaj M, Ruhai P, and Mittal R (2017). Role of glutathione-S-transferases in neurological problems. *Expert Opin. Ther. Pat* 27, 299–309. [PubMed: 27785931]
- Lachman HM, Fann CSJ, Bartzis M, Evgrafov OV, Rosenthal RN, Nunes EV, Miner C, Santana M, Gaffney J, Riddick A, et al. (2007). Genomewide suggestive linkage of opioid dependence to chromosome 14q. *Hum. Mol. Genet* 16, 1327–1334. [PubMed: 17409192]
- Leung A, and Chue P (2000). Sex differences in schizophrenia, a review of the literature. *Acta Psychiatr. Scand. Suppl* 401, 3–38. [PubMed: 10887978]
- Lévi S, Grady RM, Henry MD, Campbell KP, Sanes JR, and Craig AM (2002). Dystroglycan is selectively associated with inhibitory GABAergic synapses but is dispensable for their differentiation. *J. Neurosci* 22, 4274–4285. [PubMed: 12040032]
- Liu Q-R, Drgon T, Johnson C, Walther D, Hess J, and Uhl GR (2006). Addiction molecular genetics: 639,401 SNP whole genome association identifies many “cell adhesion” genes. *Am. J. Med. Genet. B. Neuropsychiatr. Genet* 141B, 918–925. [PubMed: 17099884]
- Liu C, Kershberg L, Wang J, Schneeberger S, and Kaeser PS (2018). Dopamine secretion is mediated by sparse active zone-like release sites. *Cell* 172, 706–718.e15. [PubMed: 29398114]
- Lukacsovich D, Winterer J, Que L, Luo W, Lukacsovich T, and Földy C (2019). Single-cell RNA-seq reveals developmental origins and ontogenetic stability of neurexin alternative splicing profiles. *Cell Rep.* 27, 3752–3759.e4. [PubMed: 31242409]
- Maslarova A, Lippmann K, Salar S, Rösler A, and Heinemann U (2015). Differential participation of pyramidal cells in generation of spontaneous sharp wave-ripples in the mouse subiculum in vitro. *Neurobiol. Learn. Mem* 125, 113–119. [PubMed: 26318491]
- Nguyen T-M, Schreiner D, Xiao L, Traunmüller L, Bornmann C, and Scheiffele P (2016). An alternative splicing switch shapes neurexin repertoires in principal neurons versus interneurons in the mouse hippocampus. *eLife* 5, e22757. [PubMed: 27960072]
- Novak G, Boukhadra J, Shaikh SA, Kennedy JL, and Le Foll B (2009). Association of a polymorphism in the NRXN3 gene with the degree of smoking in schizophrenia: A preliminary study. *World J. Biol. Psychiatry* 10, 929–935. [PubMed: 19658047]
- Que L, Lukacsovich D, Luo W, and Földy C (2021). Transcriptional and morphological profiling of parvalbumin interneuron subpopulations in the mouse hippocampus. *Nat. Commun* 12, 108. [PubMed: 33398060]
- Restrepo S, Langer NJ, Nelson KA, and Aoto J (2019). Modeling a neurexin-3 α human mutation in mouse neurons identifies a novel role in the regulation of transsynaptic signaling and neurotransmitter release at excitatory synapses. *J. Neurosci* 39, 9065–9082. [PubMed: 31578233]
- Ribeiro LF, Verpoort B, Nys J, Vennekens KM, Wierda KD, and de Wit J (2019). SorCS1-mediated sorting in dendrites maintains neurexin axonal surface polarization required for synaptic function. *PLoS Biol.* 17, e3000466. [PubMed: 31658245]
- Schlingloff D, Káli S, Freund TF, Hájos N, and Gulyás AI (2014). Mechanisms of sharp wave initiation and ripple generation. *J. Neurosci* 34, 11385–11398. [PubMed: 25143618]
- Sterky FH, Trotter JH, Lee S-J, Recktenwald CV, Du X, Zhou B, Zhou P, Schwenk J, Fakler B, and Südhof TC (2017). Carbonic anhydrase-related protein CA10 is an evolutionarily conserved pan-neurexin ligand. *Proc. Natl. Acad. Sci. USA* 114, E1253–E1262. [PubMed: 28154140]
- Südhof TC (2017). Synaptic neurexin complexes: A molecular code for the logic of neural circuits. *Cell* 171, 745–769. [PubMed: 29100073]
- Tabatadze N, Huang G, May RM, Jain A, and Woolley CS (2015). Sex differences in molecular signaling at inhibitory synapses in the hippocampus. *J. Neurosci* 35, 11252–11265. [PubMed: 26269634]

- Taniguchi H, He M, Wu P, Kim S, Paik R, Sugino K, Kvitsiani D, Fu Y, Lu J, Lin Y, et al. (2011). A resource of Cre driver lines for genetic targeting of GABAergic neurons in cerebral cortex. *Neuron* 71, 995–1013. [PubMed: 21943598]
- Trotter JH, Hao J, Maxeiner S, Tsetsenis T, Liu Z, Zhuang X, and Südhof TC (2019). Synaptic neurexin-1 assembles into dynamically regulated active zone nanoclusters. *J. Cell Biol* 218, 2677–2698. [PubMed: 31262725]
- Uchigashima Motokazu, Konno Kohtarou, Demchak Emily, Cheung Amy, Watanabe Takuya, Kenner David, Abe Manabu, Le Timmy, Sakimura Kenji, Sasaoka Toshikuni, Uemura Takeshi, Kawasaki Yuka, Watanabe Masahiko, and Futai Kensuke (2020). Specific Neuroligin3- α Neurexin1 signaling regulates GABAergic synaptic function in mouse hippocampus. *Elife* 9, e59545. 10.7554/eLife.59545. [PubMed: 33355091]
- Ullrich B, Ushkaryov YA, and Südhof TC (1995). Cartography of neurexins: More than 1000 isoforms generated by alternative splicing and expressed in distinct subsets of neurons. *Neuron* 14, 497–507. [PubMed: 7695896]
- Wee RWS, and MacAskill AF (2020). Biased connectivity of brain-wide inputs to ventral subiculum output neurons. *Cell Rep.* 30, 3644–3654.e6. [PubMed: 32187537]
- Wozny C, Maier N, Schmitz D, and Behr J (2008). Two different forms of long-term potentiation at CA1-subiculum synapses. *J. Physiol* 586, 2725–2734. [PubMed: 18403426]
- Zhang B, Chen LY, Liu X, Maxeiner S, Lee S-J, Gokce O, and Südhof TC (2015). Neuroligins sculpt cerebellar purkinje-cell circuits by differential control of distinct classes of synapses. *Neuron* 87, 781–796. [PubMed: 26291161]
- Zhang M, Zhou Y, Jiang Y, Lu Z, Xiao X, Ning J, Sun H, Zhang X, Luo H, Can D, et al. (2021). Profiling of sexually dimorphic genes in neural cells to identify *Eif2s3y*, whose overexpression causes autism-like behaviors in male mice. *Front. Cell Dev. Biol* 9, 669798. [PubMed: 34307355]

Highlights

- PV circuits in ventral subiculum are organized sex specifically
- Nrnx3 function in PV interneurons depends on postsynaptic cell identity
- Nrnx3 has distinct functions at PV-RS synapses in female mice compared to males
- Nrnx3 suppresses presynaptic release at female PV-RS synapses

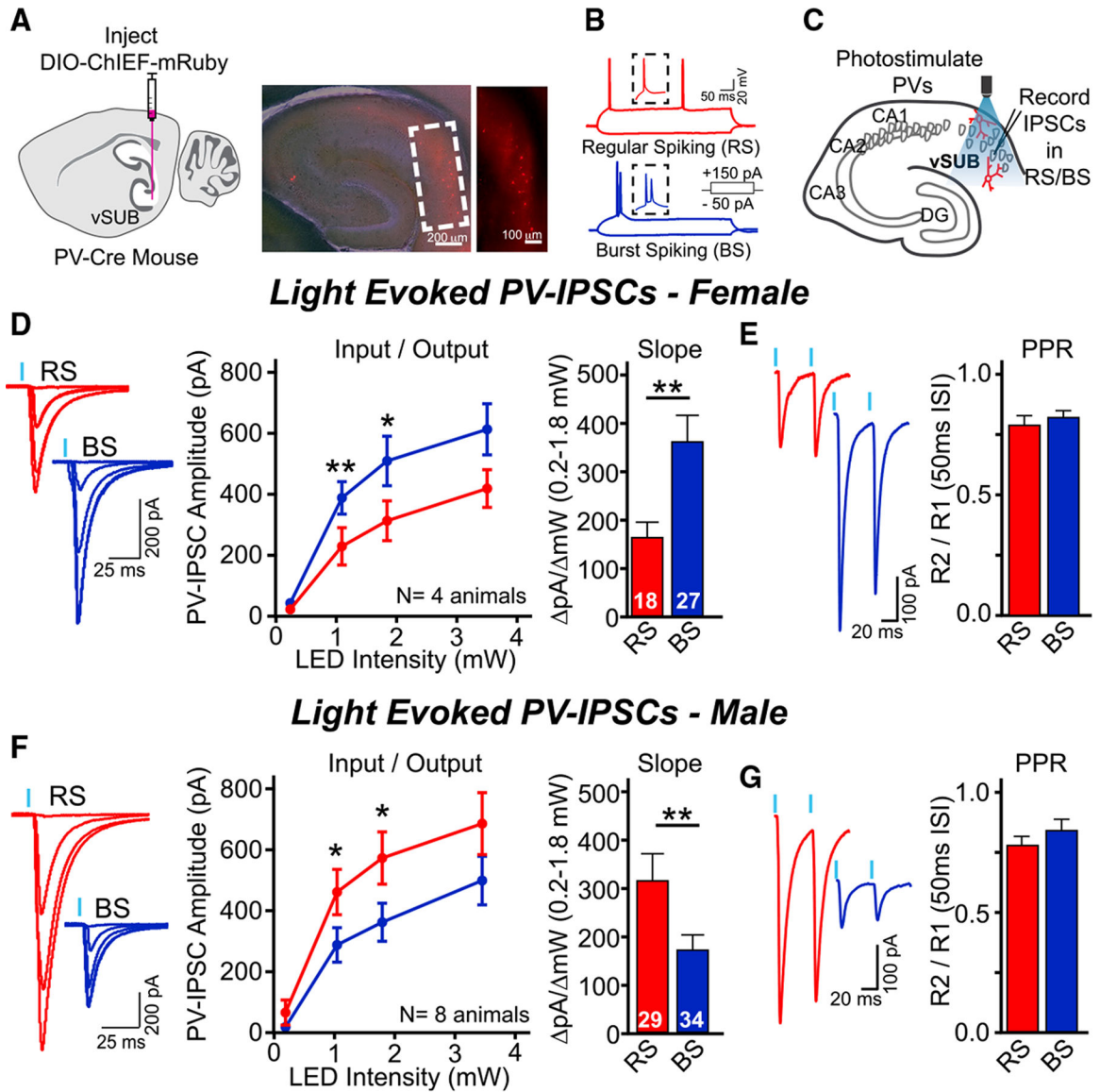


Figure 1. PV interneurons exhibit cell-type- and sex-dependent inhibitory bias in the basal subicular microcircuit

(A) Diagram of AAV injection of Cre-dependent ChIEF into vSUB of PV-Cre mouse (left) and example image of ChIEF-mRuby expression in vSUB PV neurons. Scale bar, 200 μ m. Inset: magnified vSUB (scale bar, 100 μ m).

(B) Identification of regular-spiking (RS) and burst-spiking (BS) cells recorded in current clamp mode. Insets: Expanded view of single versus double (burst) action potentials.

(C) Recording configuration: PV neurons (red) are optogenetically activated with a 473-nm LED light, eliciting PV-IPSCs recorded in RS/BS neurons.

(D) In females, PV-synaptic drive is significantly greater onto BS compared to RS neurons. Representative PV-IPSCs (left), input/output (I/O) curves (middle), and corresponding I/O slopes (right) of light-evoked PV-IPSC amplitudes in RS and BS neurons. Mann-Whitney test (RS versus BS) at 1.1, 1.8, and 3.5 mW: $p = 0.006$, $p = 0.011$, and $p = 0.074$; slope, $p = 0.001$ (t test).

(E) Representative traces (left) and quantification (right) of light-evoked PPRs from RS and BS neurons. t test (RS versus BS), $p = 0.825$

(F and G) Same as in (D) and (E) but in males. Unlike females, PV-IPSC inhibitory drive is greater onto RS neurons compared to BS neurons. Mann-Whitney test (RS versus BS) at 1.1, 1.8, and 3.5 mW: $p = 0.031$, $p = 0.019$, and $p = 0.156$; slope, $p = 0.007$ (t test); PPR, $p = 0.063$ (t test).

Data points in I/O curves and bar graphs are represented as mean \pm SEM; numbers in bars are cell numbers, $N = 4$ animals (female), $N = 8$ animals (male). Note that these data were obtained from control experiments performed in Figure 4.

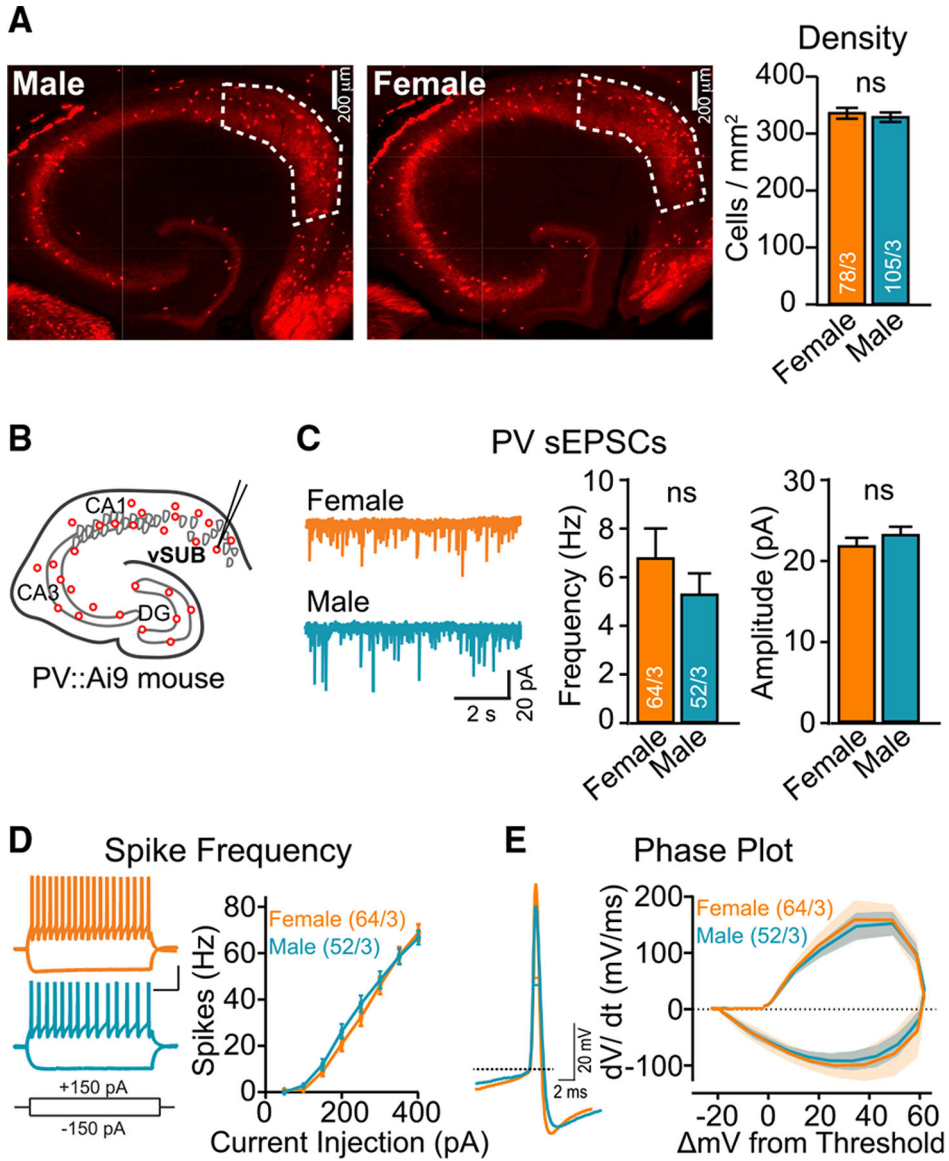


Figure 2. Intrinsic properties of PV interneurons do not exhibit sexual dimorphism

(A) (Left) Images of ventral hippocampal slices (30 μm thick) made from PV-Cre::Ai9 mice with vSUB quantification region outlined. Scale bars, 200 μm . (Right) Quantification of tdTomato⁺ PV neuron density in vSUB region. n/N = slice/animal, animal means compared (male [M] versus female [F], t test): $p = 0.611$. Scale bar, 200 μm .

(B) Schematic of whole-cell electrophysiology recordings of tdTomato⁺ PV neurons in vSUB.

(C) Representative traces of spontaneous EPSCs recorded in PV cells (left) and bar graphs of average frequency and amplitude (right) of male and female PV sEPSC events. Mann-Whitney test for males versus females: frequency, $p = 0.904$; amplitude, $p = 0.181$

(D) (Left) Examples of physiological responses of female (top) and male (bottom) fast-spiking, tdTomato⁺ PV interneurons to current injections of 150 and -150 pA. Scale bars, 100 ms by 35 mV. (Right) Summary plot of male and female PV neuron spike frequency to

increasing levels of current injection. Mann-Whitney test for males versus females: 200 pA, $p = 0.235$; 250 pA, $p = 0.2826$; 300 pA, $p = 0.635$.

(E) (Left) Example traces of single PV action potentials (male and female overlaid). (Right) Mean phase plots and standard error produced from single PV action potentials.

Summary data are mean \pm SEM; numbers in bar graphs and plots (C and D) are n/N (cells/animals). See also Table S1.

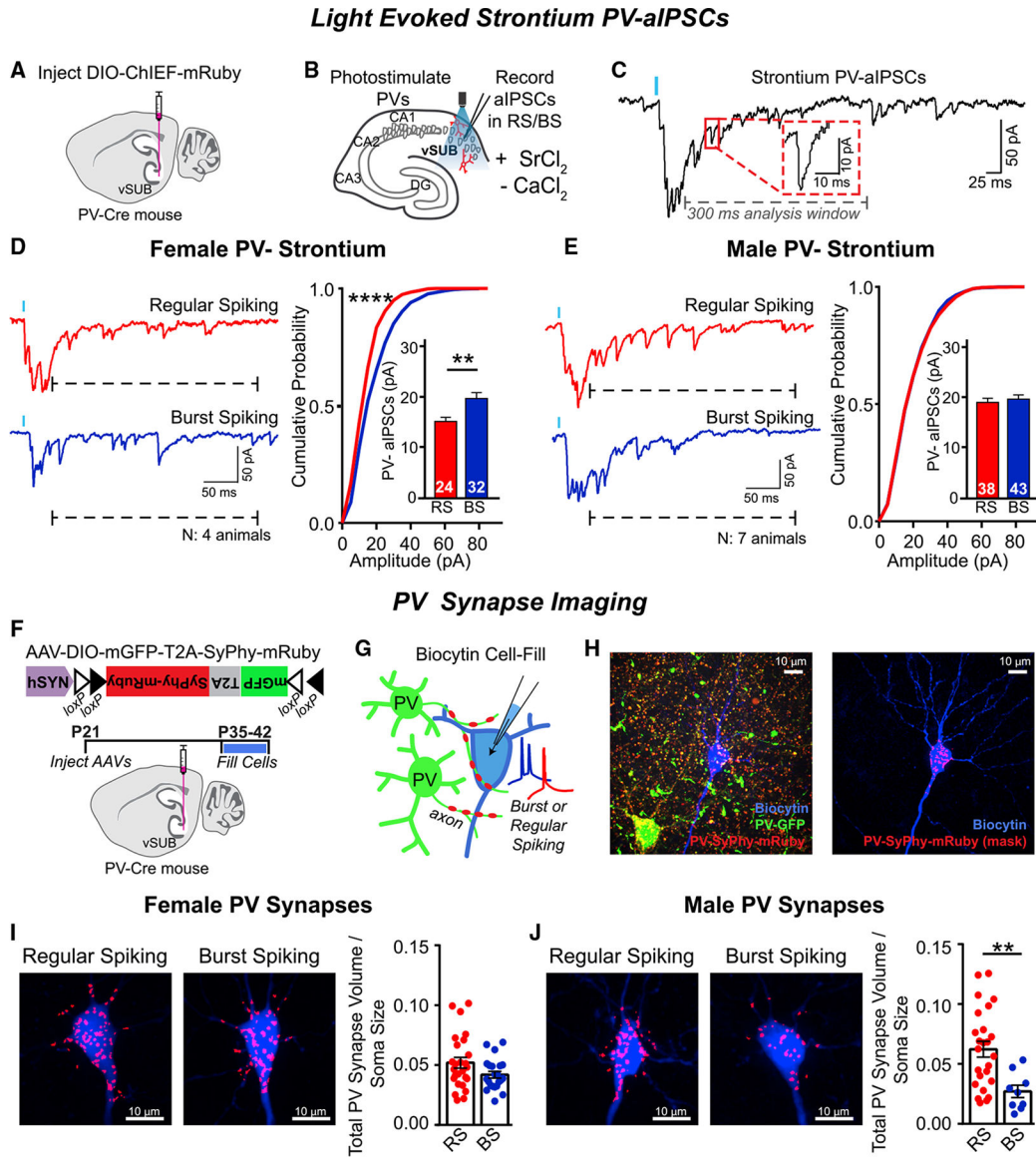


Figure 3. Sex-specific patterning of vSUB PV-RS and PV-BS preference is mediated by synaptic density in males and postsynaptic strength in females

(A) Schematic of AAV injection of Cre-dependent ChIEF into vSUB of PV-Cre mouse.

(B) Schematic of recording configuration: Strontium desynchronizes GABA release in PV neurons optogenetically activated with 473-nm LED light, eliciting PV-aIPSCs in RS/BS neurons.

(C) Example of a light-evoked response in strontium artificial cerebrospinal fluid (ACSF). Note that asynchronous PV-iPSCs occur for hundreds of milliseconds following a small phasic PV-IPSC (first 300 ms were analyzed). Red box shows an enlarged, single aIPSC event.

(D) PV-aIPSC amplitude is larger in BS compared to RS neurons in females (N = 4). Representative traces (left), cumulative probability plots (right) of PV-aIPSC amplitude distribution, and bar graphs of mean PV-aIPSC amplitudes (inset) from RS and BS neurons.

$p = 0.005$ (t test), $p < 0.0001$ (Kolmogorov-Smirnov [KS] test). KS test $n(\text{RS}, \text{BS}) = 717,1292$ events.

(E) Same as (D) but in males ($N = 7$); PV-aIPSC amplitude is equal between RS and BS neurons. $p = 0.935$ (t test); $p = 0.945$ (KS test). KS test $n(\text{RS}, \text{BS}) = 699,1398$ events.

(F) (Top) Diagram of the cre-dependent AAV utilized for PV-synaptic bouton labeling. (Bottom) Experimental timeline and schematic of AAV injection into vSUB.

(G) Schematic of mRuby-labeled PV synapses and cell filling in *ex vivo* slices. PV neurons (expressing GFP and synaptophysin-mRuby) make synaptic contacts onto an electrophysiologically identified and biocytin-filled pyramidal neuron in vSUB.

(H) (Left) Maximum-projected image of a principal neuron (blue) and a neighboring PV neuron (green) in a vSUB slice expressing AAV (see above). (Right) Same image but showing somatic PV and mRuby-positive puncta masks (red), which were utilized in the final quantifications (below). Scale bars, 10 μm .

(I) Representative maximum-projected images (left) and summary graphs representing the average total PV synaptic volume normalized to soma volume (right) of PV synapse density on RS and BS somas in females. RS/BS: $n = 26/22$ cells, $n = 6$ animals; $p = 0.073$ (t test). Scale bars, 10 μm .

(J) Same as (I) but in males. PV synapse density is significantly greater onto RS compared to BS somas in males. RS/BS: $n = 25/9$ cells, $n = 4$ animals; $p = 0.004$ (t test). Scale bars, 10 μm .

Data in bar graphs are represented as mean \pm SEM. Numbers within bars (graphs D and E) represent the number of cells. RS versus BS (bar graphs) statistically compared by Student's t test or a Mann-Whitney test. Cumulative probability plots compared using a KS test.

** $p < 0.01$, **** $p < 0.0001$. Note that these data were obtained from control experiments performed in Figure 6. See also Figure S1.

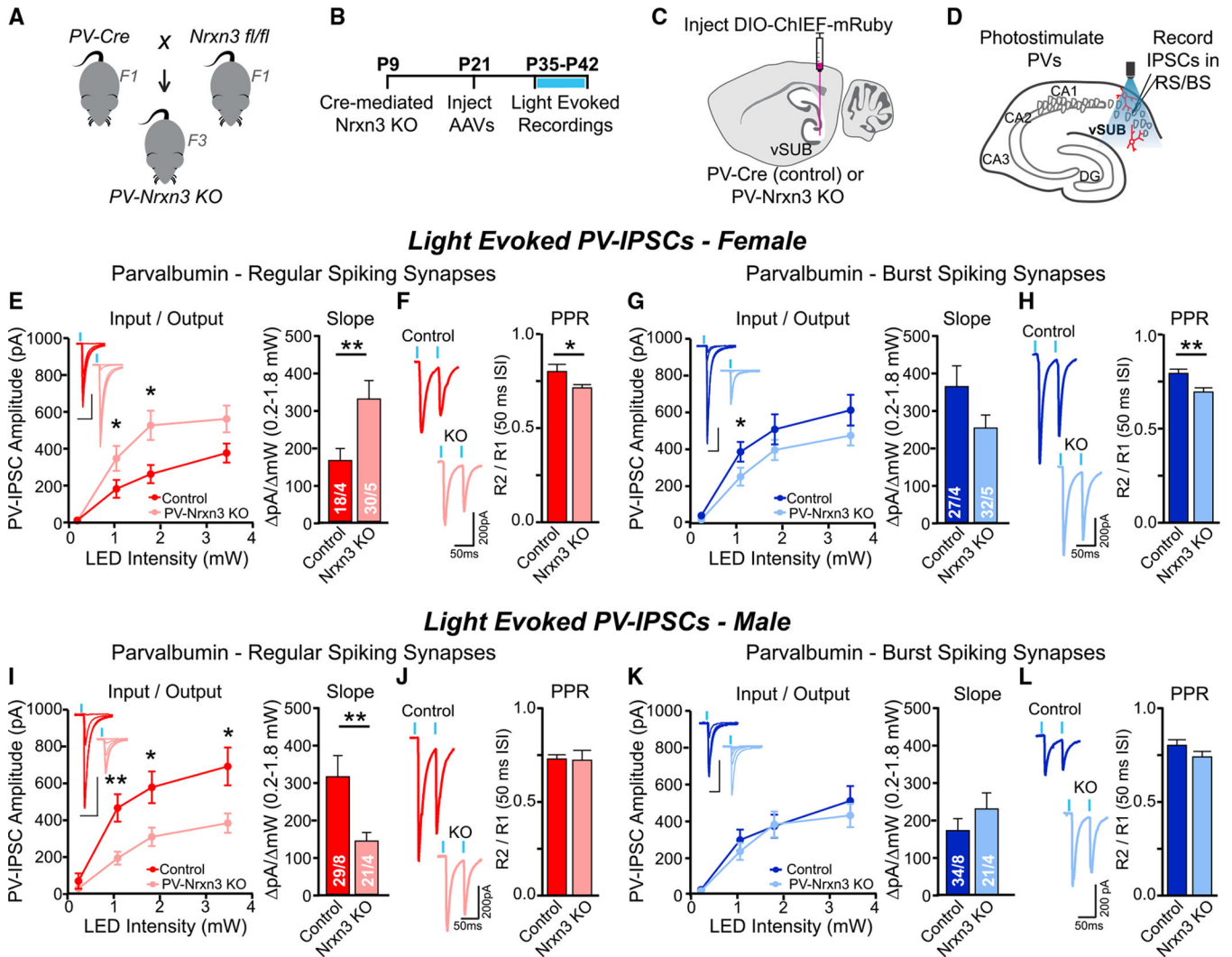


Figure 4. Nrnx3 exerts sex-dependent and synapse-specific effects at PV-RS and PV-BS synapses in vSUB

(A) Breeding scheme to produce PV-Cre::Nrnx3^{fl/fl} (PV-Nrxn3 KO) mice.

(B) Experimental timeline: PV promoter becomes active at ~P9, causing Cre-mediated excision of Nrnx3 in PV-Nrxn3 KO mice.

(C) Schematic of AAV injection of DIO ChIEF-mRuby into vSUB of PV-Cre (control) or PV-Nrxn3 KO animals.

(D) Schematic of recording configuration: PV neurons are optogenetically activated with 473-nm LED light, eliciting PV-IPSCs in RS/BS neurons.

(E) PV-Nrxn3 KO enhances female PV-IPSCs in RS neurons. I/O curves (left), representative traces (inset), and slopes (right) of PV-IPSCs in RS neurons from control and PV-Nrxn3 KO animals are shown. Mann-Whitney test (control versus KO) at 1.1, 1.8, and 3.5 mW: $p = 0.041$, $p = 0.010$, and $p = 0.197$; slope, $p = 0.005$ (t test).

(F) Release probability is enhanced in PV-Nrxn3 KO females. Representative traces (left) and quantification (right) of paired-pulse responses at PV-RS synapses in control and PV-Nrxn3 KO animals. $p = 0.0256$ (t test).

(G and H) Same as (E) and (F) but in BS neurons. PV-IPSCs in BS neurons are not significantly altered in PV-Nrxn3 KO females. Mann-Whitney test (control versus KO) at 1.1, 1.8, and 3.5 mW: $p = 0.031$, $p = 0.280$, and $p = 0.247$; slope, $p = 0.064$ (t test); PPR, $p = 0.004$ (t test).

(I and J) Same as (E) and (F) but in males. PV-Nrxn3 KO impairs PV-IPSCs in RS neurons (I) without altering PPR (J). Mann-Whitney test (control versus KO) at 1.1, 1.8, and 3.5 mW: $p = 0.001$, $p = 0.043$, and $p = 0.024$; slope, $p = 0.006$ (t test); PPR, $p = 0.906$ (t test).

(K and L) Same as (G) and (H) but in males. PV-Nrxn3 KO does not impact PV-IPSC amplitude (K) or PPR in male BS neurons (L). Mann-Whitney test (control versus KO) at 1.1, 1.8, and 3.5 mW: $p = 0.962$, $p = 0.650$, and $p = 0.861$; slope, $p = 0.445$ (t test); PPR, $p = 0.156$ (t test).

Data points in I/O and bar graphs are represented as mean \pm SEM; numbers in bars represent n/N number of cells/animals. Scale bars, 50 ms by 200 pA. * $p < 0.05$, ** $p < 0.01$. Note that the control data obtained from these experiments are also presented in Figure 1 to directly compare RS versus BS for basal circuit characterization. See also Figure S2.

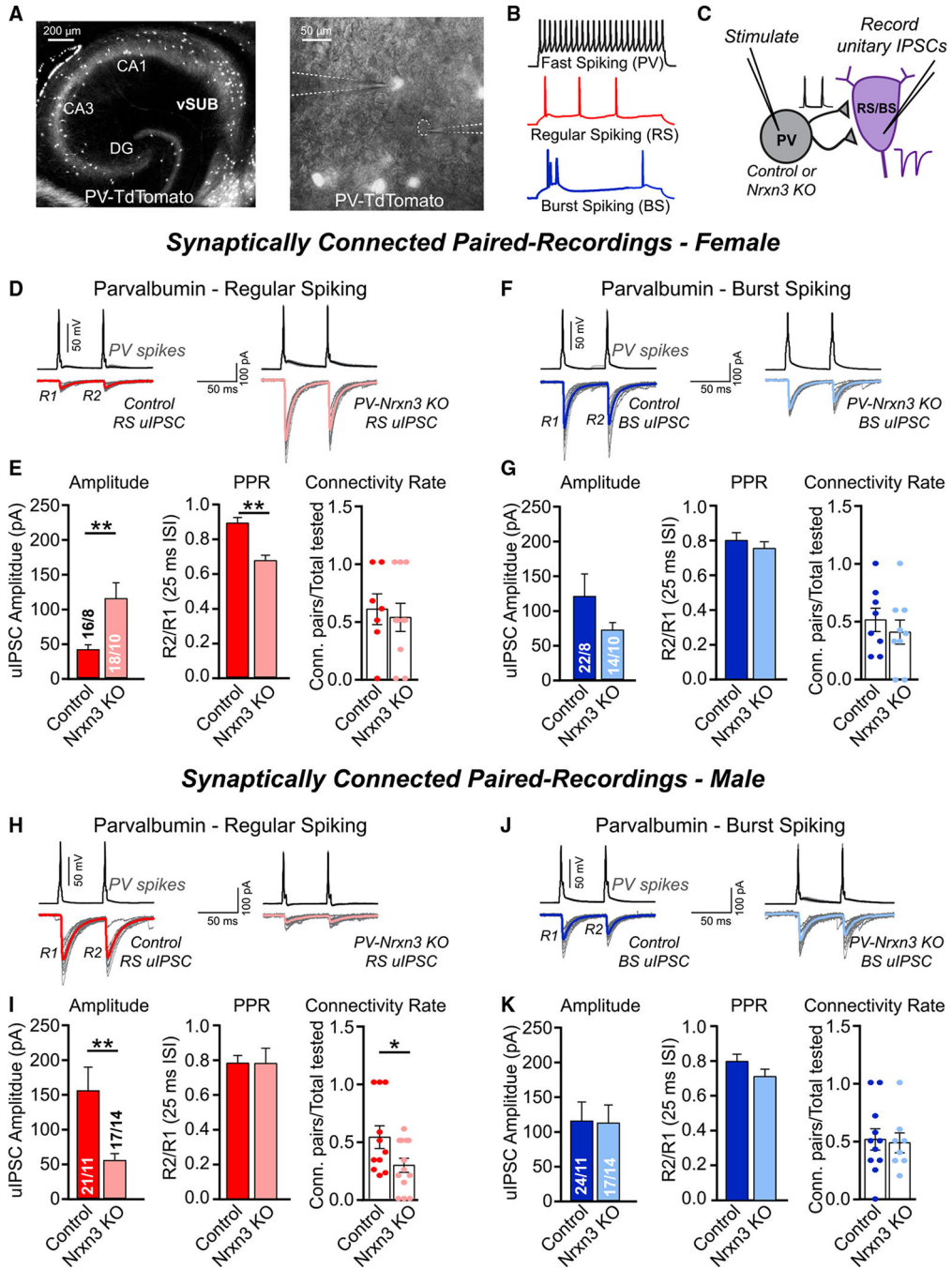


Figure 5. Synaptically connected paired recordings reveal sex- and synapse-specific roles of PV Nrnx3

(A) Image of tdTomato⁺ PV neurons in ventral hippocampus from a PV-Cre::Ai9 animal (left; scale bar, 200 μ m) and fluorescent image overlaid on bright-field image of a paired recording (PV neuron-BS neuron) in vSUB of an *ex vivo* slice (right; scale bar, 50 μ m). (B) Intrinsic firing patterns used to identify fast-spiking PV neurons (top) and regular (middle) and burst spiking (bottom) pyramidal neurons. (C) Illustration of synaptically connected paired recording: presynaptic PV neurons with intact Nrnx3 (control) or Nrnx3 deletion (PV-Nrxn3 KO) are fired with current injections,

and resulting PV-unitary IPSCs (uIPSCs) are recorded in postsynaptic RS or BS pyramidal neurons.

(D) Representative PPR traces: PV action potentials (black) result in uIPSCs in synaptically connected RS neurons from PV-Cre (control, left) and PV-Nrxn3 KO female animals (right). Average trace is shown overlaid on multiple trials (gray).

(E) uIPSC amplitude and release probability are enhanced in RS neurons in PV-Nrxn3 KO female animals. Quantification is shown of mean uIPSC amplitude (left), PPR (middle), and connectivity rate (Conn. rate) (right) of PV-RS pairs in control and PV-Nrxn3 KO female animals. Control versus KO: amplitude, $p = 0.002$ (Mann-Whitney test); PPR, $p < 0.0001$ (t test); Conn. rate, $p = 0.705$ (t test).

(F and G) Same as (D) and (E) but comparing PV-BS pairs from control and PV-Nrxn3 KO female animals. Control versus KO: amplitude, $p = 0.962$ (Mann-Whitney test); PPR, $p = 0.622$ (Mann-Whitney test); Conn. rate, $p = 0.481$ (t test).

(H and I) Same as (D) and (E) but in males. PV-Nrxn3 KO results in a loss-of-function phenotype at PV-RS synapses. Control versus KO: amplitude, $p = 0.002$ (Mann-Whitney test); PPR, $p = 0.987$ (t test); Conn. rate, $p = 0.039$ (t test).

(J and K) Same as in (F) and (G) but at male PV-BS synapses. Control versus KO: amplitude, $p = 0.824$ (Mann-Whitney test); PPR, $p = 0.209$ (t test); Conn. rate, $p = 0.699$ (Mann-Whitney test).

Data in bar graphs are represented as mean \pm SEM; numbers in bars represent number of pairs/animals; dots on connectivity rate plots represent individual animals. See also Figure S3.

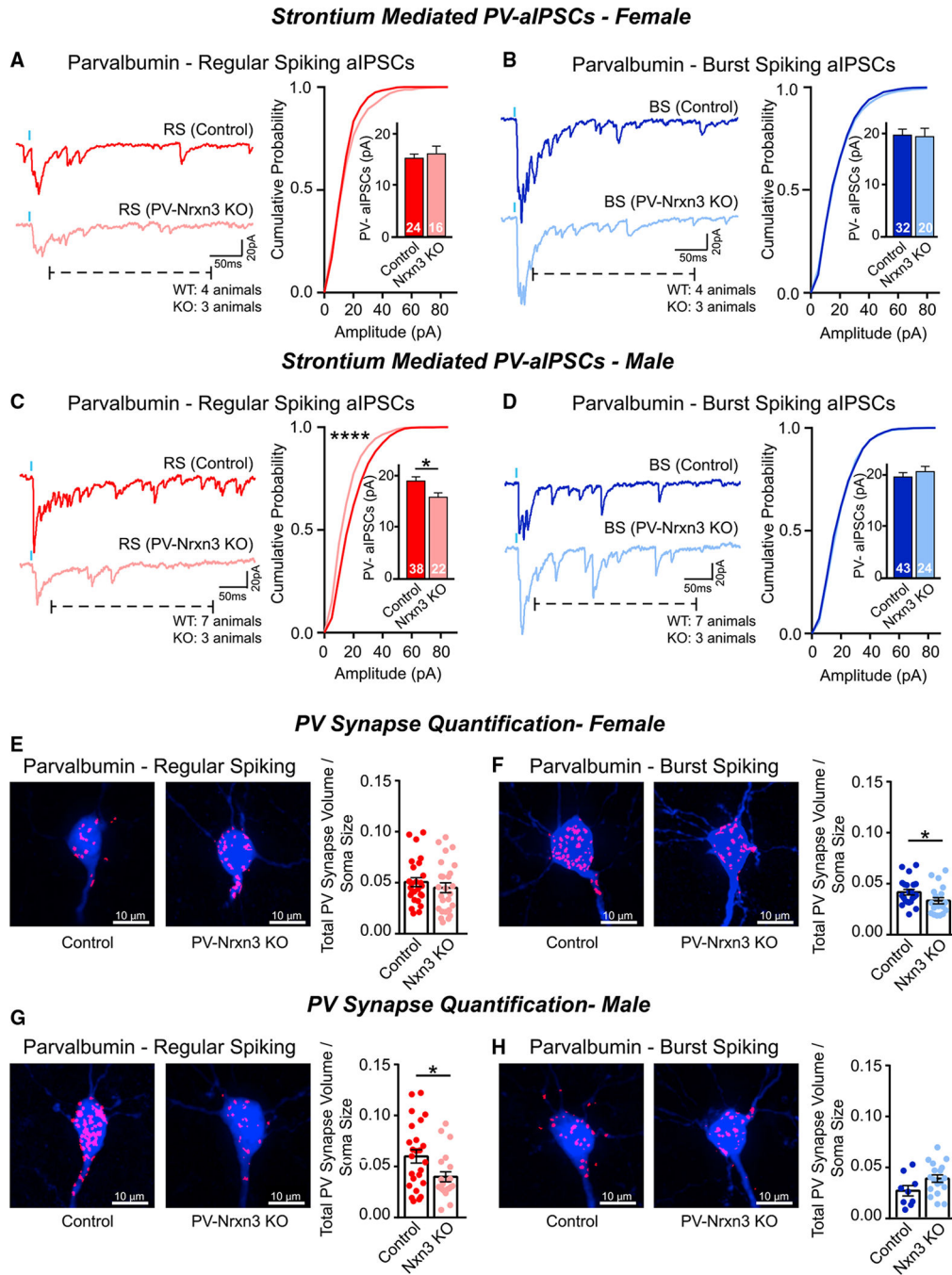


Figure 6. Nrxn3 controls PV synapse number in a cell-type- and sex-dependent manner (A–D) Assessment of PV inhibitory postsynaptic strength, measured by light-evoked, strontium-mediated asynchronous IPSCs (PV-aIPSCs) in female (A and B) and male (C and D) RS and BS synapses. Female: RS, $p = 0.95$ (Mann-Whitney test), $p = 0.075$ (KS test); BS, $p = 0.88$ (t test), $p = 0.471$ (KS test). KS test $n(\text{RS}, \text{KO}, \text{BS}, \text{KO}) = 717, 1292, 490, 919$ events. (C and D) Male: RS, $p = 0.021$ (t test), $p < 0.0001$ (KS test); BS, $p = 0.523$ (t test), $p = 0.189$ (KS test). KS test $n(\text{RS}, \text{KO}, \text{BS}, \text{KO}) = 699, 589, 1398, 881$ events.

(E–H) PV-Cre (control) and PV-Nrxn3 KO animals were injected with AAV-DIO-mGFP-T2A-synaptophysin-mRuby and then PV synapses made RS/BS neurons were quantified (see Figures 4F and 4G). Female (E and F): control versus KO: RS, $p = 0.402$; BS, $p = 0.047$ (t test). $N(\text{control RS/BS}) = 26/22$ cells/6 mice; $N(\text{KO RS/BS}) = 26/20$ cells/6 mice. Scale bars, 10 μm .

(G and H) Male (G and H): control versus KO: RS, $p = 0.021$; BS, $p = 0.07$ (t test).

$N(\text{Control RS/BS}) = 25/9$ cells/4 mice; $\text{KO} = 21/18$ cells/5 mice.

Data in bar graphs are represented as mean \pm SEM; numbers in bar graphs represent number of cells. Cumulative probability plots were compared using KS test. For cumulative plots:

* $p < 0.05$, **** $p < 0.0001$; ns, not significant ($p > 0.05$). Note that the control data from these experiments are also presented in Figure 3 to directly compare RS versus BS for basal circuit characterization. See also Figure S4.

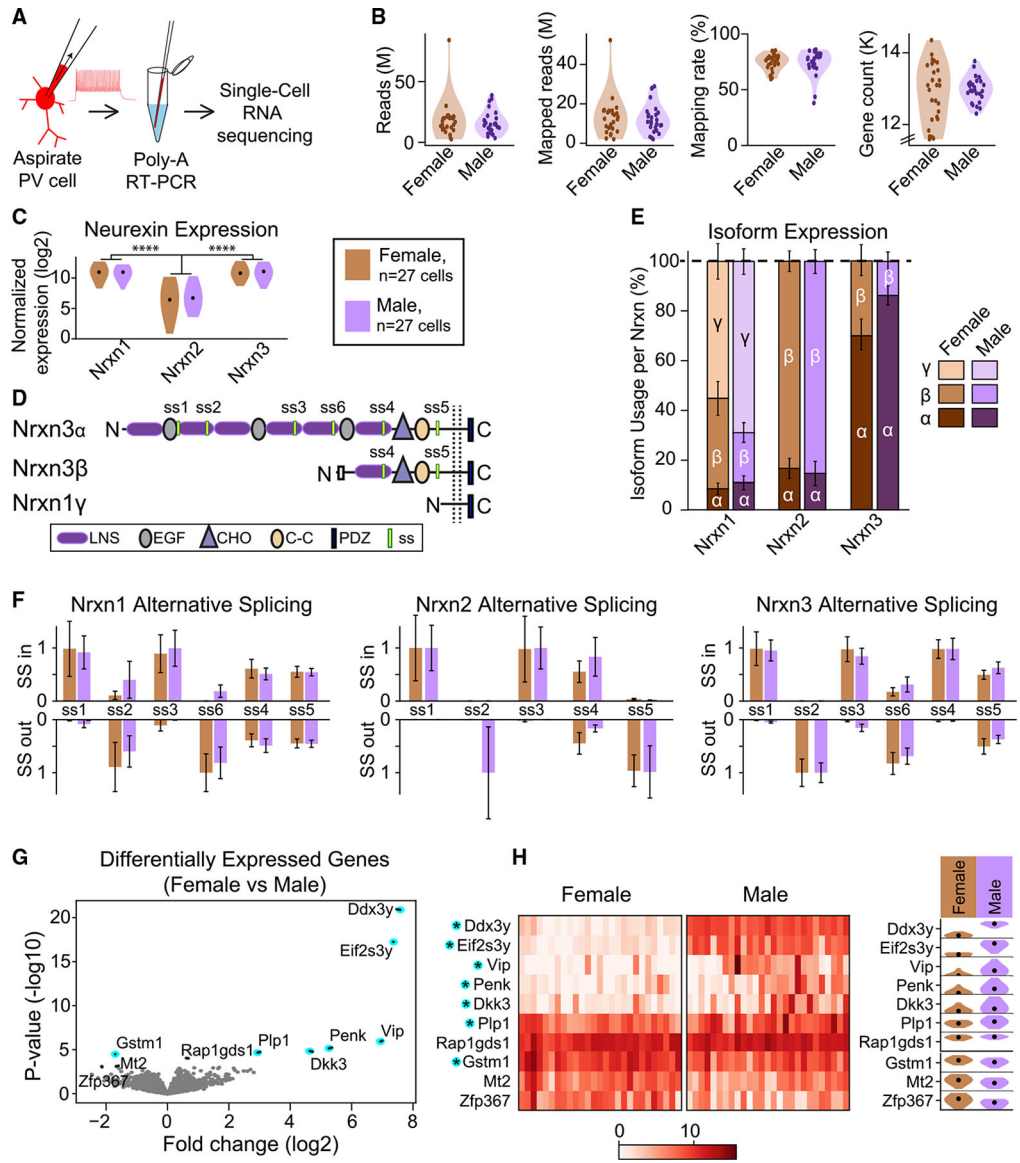


Figure 7. Neurexin isoform expression and alternative splicing in vSUB PVs are comparable between sexes

(A) Experimental steps. Fast-spiking tdTomato⁺ PV neurons were aspirated from male and female vSUB slices and then processed individually for RNA sequencing.

(B) Violin plots representing the total number of mRNA reads and mapped reads to mouse genome (in millions), mapping rate, and total gene count (in thousands) from female and male PV neurons.

(C) Violin plots comparing log-transformed expression levels of Nrnx1–3 in males and females. Nrnx1 and Nrnx3 are highly expressed compared to Nrnx2 ($p < 0.0001$, Welch test), but no differences were found between females versus males.

(D) Schematic of Nrnx3 α , Nrnx3 β , and Nrnx1-specific γ structures with splice sites (ss) 1–6 labeled.

(E) Stacked bar plots showing male/female isoform expression levels as a percentage of total for each Nrnx1–3. Note that while isoform expression varies between Nrnx1, Nrnx2, and

Nrxn3, relative expression patterns between females and males are comparable. See also Figure S5B for total isoform expression levels.

(F) Bar plots indicating mean ratio of splice site (ss) inclusion (up) versus exclusion (down) for Nrxn1–3 in males and females. No significant differences were found between male versus female.

(G) Volcano plot comparing gene expression in female versus male PV neurons with top 10 differentially expressed genes labeled, and statistical significance ($FDR < 0.05$) indicated by cyan dot.

(H) Heatmap to denote expression levels of each PV cell of the top 10 differentially expressed genes between female versus male (left) and corresponding violin plots (right) showing mean and distribution.

Data in bar graphs are represented as mean \pm SEM. Female, $n = 27/3$; male: $n = 27/4$ (cells/mice). Welch tests were used to compare female versus male expression levels for (C) and (E). In (C), male and female expression values were pooled, then Nrxn1 versus Nrxn2 and Nrxn3 versus Nrxn2 expression was compared. A quasi-likelihood F test (EdgeR) was used to compare female versus male in (G). See also Figures S5 and S6.

KEY RESOURCES TABLE

REAGENT or RESOURCE	SOURCE	IDENTIFIER
Antibodies		
Cy5-conjugated Streptavidin	Jackson ImmunoResearch	016-170-084; RRID: AB_2337245; Lot: 138512
DyLight 405-conjugated Streptavidin	Jackson ImmunoResearch	016-470-084; RRID: AB_2337248; Lot: 154739
Parvalbumin antibody (polyclonal guinea pig)	Immunostar	Cat# 24428; RRID: AB_572259; Lot: 1706001
Neuroigin 2 antibody (monoclonal mouse)	Synaptic Systems	Cat# 129511; RRID: AB_2619813
Neuroigin 3 antibody (rabbit)	Budreck and Scheiffele, 2007	N/A
Cy2-Conjugated Affinipure Donkey Anti-Guinea Pig IgG	Jackson ImmunoResearch	706-545-148; RRID: AB_2340472; Lot: 146642
Cy3-Conjugated Affinipure Donkey Anti-Mouse IgG	Jackson ImmunoResearch	715-165-151; RRID: AB_2315777
Alexa Fluor 647-Conjugated Affinipure Donkey Anti-Rabbit IgG	Jackson ImmunoResearch	711-605-152; RRID: AB_2492288; Lot: 145576
Bacterial and virus strains		
pAAV DJ hSyn-DIO _{LoxP} -ChIEF-mRuby	This manuscript	N/A
pAAV DJ hSyn-DIO _{LoxP} -mGFP-T2A-Synaptophysin-mRuby	Beier et al., 2015	Addgene, Plasmid #71760
pAAV DJ hSyn-DIO _{LoxP} -mRuby	This manuscript	N/A
Chemicals, peptides, and recombinant proteins		
NBQX	Hello Bio	HB0443
D-APV	Hello Bio	HB0225
Picrotoxin	Hello Bio	HB0506
Biocytin	Sigma-Aldrich	B4261
Deposited data		
PV single-cell RNA sequencing dataset	This manuscript	GEO: GSE171793
Image Analysis Code (MATLAB)	This manuscript	Zenodo: https://doi.org/10.5281/zenodo.5651193
Critical commercial assays		
Takara SMARTSeq HT	Takara	634437
Nextera XT DNA Library Preparation Kit	Illumina	FC-131-1096
Experimental models: Organisms/strains		
Mouse: Neurexin-3 α/β cKO: <i>Nrxn3^{tm3Sud/J}</i>	Gift, Dr. Thomas Südhof, Stanford University	JAX: 014157, RRID: IMSR_JAX:014157
Mouse: PV-IRES-Cre: B6;129P2- <i>Pvalb^{tm1(cre)Arbr/J}</i>	Gift, Dr. Diego Restrepo, CU Anschutz	JAX: 008069, RRID: IMSR_JAX:008069
Mouse: Gt(ROSA)26Sortm9(CAG-tdTomato)Hze (Ai9)	The Jackson Laboratory	JAX: 007909, RRID: IMSR_JAX:007909
Oligonucleotides		
Genotyping Primer Neurexin-3 α/β cKO Forward AATAGCAGAGGGGTGTGACAC	Aoto et al., 2015	N/A
Genotyping Primer Neurexin-3 α/β cKO Reverse CGTGGGGTATTACGGATGAG	Aoto et al., 2015	N/A
Genotyping Primer Cre Forward GCCTGCATTACCGGTGCGATGCAACGA	This manuscript	N/A

REAGENT or RESOURCE	SOURCE	IDENTIFIER
Genotyping Primer Cre Reverse GTGGCAGATGGCGCGCAACACCATT	This manuscript	N/A
Genotyping Primer TdTomato WT Forward AAGGGAGCTGCAGTGGAGTA	This manuscript	N/A
Genotyping Primer TdTomato WT Reverse CCGAAAATCTGTGGGAAGTC	This manuscript	N/A
Genotyping Primer TdTomato KI Forward GCACCACGCGAGGCGCGAGAT	This manuscript	N/A
Genotyping Primer TdTomato KI Reverse CTGTTCCGTACGGCATGG	This manuscript	N/A
Software and algorithms		
Clampfit 10	Molecular Devices	https://www.moleculardevices.com/products/axon-patch-clamp-system/acquisition-and-analysis-software/pclamp-software-suite
Prism 7	GraphPad	https://www.graphpad.com/scientific-software/prism/
MATLAB	Mathworks	https://www.mathworks.com/
Python	Python	https://www.python.org/
edgeR	Bioconductor	https://bioconductor.org/packages/release/bioc/html/edgeR.html
Fiji (ImageJ)	NIH	https://imagej.net

Author Manuscript

Author Manuscript

Author Manuscript

Author Manuscript